

Assessment of reinforcements for enhancing structural performance of cold-formed steel polygonal conical poles for antennas support

Eduardo de Miranda Batista^a , João Alfredo de Lazzari^{b*} , Gustavo Yoshio Matsubara^{a,c} ,
Michèle Schubert Pfeil^a , Renato Nascimento Elias^a 

^aCivil Engineering Program, COPPE, Federal University of Rio de Janeiro, Cidade Universitária, Ilha do Fundão, C.P. 68506, Rio de Janeiro, RJ 21945-972, Brazil. Email: batista@coc.ufrj.br, gustavoyoshio@coc.ufrj.br, mpfeil@coc.ufrj.br, rnelias@nacad.ufrj.br.

^bCERIS, Instituto Superior Técnico, Universidade de Lisboa, Av. Rovisco Pais 1, 1049-001 Lisboa, Portugal. Email: joao.lazzari@tecnico.ulisboa.pt

^cDepartment of Civil Engineering, State University of Maringá, Maringá, PR 87020-900, Brazil. Email: gustavoyoshio@coc.ufrj.br

* Corresponding author

<https://doi.org/10.1590/1679-7825/e8033>

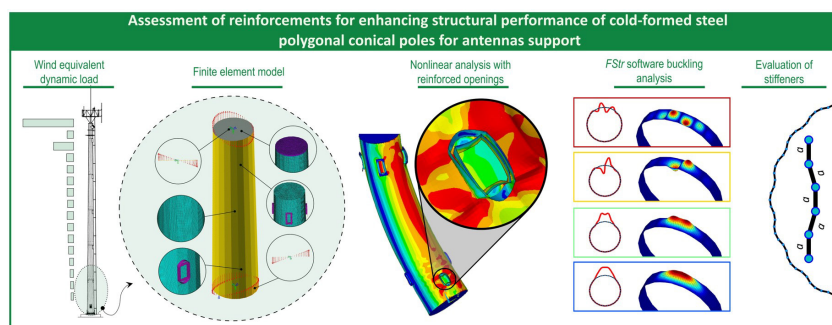
Abstract

The objective of this research is to present practical solutions for improving structural performance of thin-walled conic polygonal monopoles. The analysis encompasses computational simulations, analytical evaluation, and structural verification of reinforcements for openings and longitudinal folded stiffeners of flat walls. A benchmarked solution is derived from a design involving a 20-sided cold-formed steel polygonal section employed to support telecommunication antennas at a height of 40 meters. The structural verification is performed under the influence of wind loads, with particular attention to the commonly reported basic gust wind speed in Brazil. The conducted analysis encompasses: (i) wind-induced static equivalent dynamic behavior, (ii) parametric elastic buckling analysis, (iii) non-linear finite element analysis of reinforced openings, and (iv) direct strength method (DSM) performance evaluation of stiffened polygonal cross-sections. The importance of combining tailored numerical tools such as the finite strip and finite element methods, as well as wind-induced behavior, is demonstrated through the structural analysis results. In essence, the study's findings reveal the previously overlooked local-distortional buckling interaction in current design guidelines. Moreover, the research demonstrates that incorporating reinforcements and longitudinal stiffeners significantly enhances the flexural capacity of slender structures. Notably, the adoption of a single 4-fold (trapezoid) stiffener shape, per polygonal wall, emerges as a promising effective solution for enhancing the overall flexural capacity. Further full scale experimental structural tests and computational fluid dynamics should be considered for advanced structural analysis and improved design.

Keywords

Telecom polygonal monopole, thin-walled steel member, longitudinal polygon wall stiffener, reinforcement of openings, shell finite element analysis

Graphical Abstract



Received: jun. 2, 2024, In revised form: nov. 08, 2024, Accepted: nov. 13, 2024, Available online: nov. 14, 2024

<https://doi.org/10.1590/1679-7825/e8033>



Latin American Journal of Solids and Structures. ISSN 1679-7825. Copyright © 2025. This is an Open Access article distributed under the terms of the [Creative Commons Attribution License](https://creativecommons.org/licenses/by/4.0/), which permits unrestricted use, distribution, and reproduction in any medium, provided the original work is properly cited.

1 INTRODUCTION

1.1 Background

The installation of a new infrastructure, including support for antennas positioned as high as 40 to 50 meters in both urban and rural regions, is required for the expansion of the internet and cell phone signals. With regard to economic development, Dholakia and Harlam (1994) and Capello and Nijkamp (1996) found that investing in telecommunications infrastructure can be justified because of the positive impact on economic development and regional performance. The challenges associated with the use of telecommunication antenna supports are linked to social, economic, and environmental conditions. The environmental loads acting on the structure (e.g., wind, ice, and seismic), as well as the poor compliance with locational planning standards and the physiological impacts of telecommunication structures on residents are reported in the following papers (Amponsah et al. 2022; Cardoni et al. 2022; Odunola et al. 2015; Travanca et al. 2013), highlighting the challenges in using this structural system.

The continual advancement of materials with higher strength and the evolution of more efficient structural systems in the field of telecommunication structures bring about changes in the mechanical behavior of such structures. This necessitates the development of innovative analysis and design approaches tailored for slender structures (Hawkins 2010; Smith 2009; Solari and Pagnini 1999; Støttrup-Andersen 2009; Sabau et al. 2018; Travanca et al. 2019). In light of these developments, as emphasized by Travanca et al. (2019), there are demands for the adoption of advanced structural design methods, including computational modeling, to address the evolving challenges in this domain.

Traditional telecommunication structural solutions are based on masts, self-supporting towers and trussed structural systems, with the latter having a much larger base area and impacting the costs of the ground occupancy. This factor is of utmost importance, which is why steel monopoles with thin-walled polygonal cross-section have been developed in an effort to find a lightweight and cost-effective solution. However, thin-walled steel polygonal conic towers encounter limitations related to instability phenomena, influenced by various factors, including:

- (i) the inclusion of openings for cable maintenance,
- (ii) changes in the number of sides and pole height directly contributing to local/distortional slenderness due to the conic structural system,
- (iii) rigidity issues in connections between modules,
- (iv) stress concentrations and fatigue effects at ground base connections and between modules, and
- (v) the flexural behavior induced by horizontal actions, such as seismic and wind loads.

1.2 Research gaps in polygonal conic monopoles: a critical examination

Godat et al. (2012) noted that there is a growing interest in the study of thin-walled steel tubular polygons. This heightened attention is attributed to their versatile applications in urban environments, serving not only for telecommunication purposes but also as structures for transmission lines and signs. Moreover, these structures present a low-cost maintenance and a better aesthetic aspect for urban environments than lattice towers. Therefore, several studies were carried out to investigate this type of structure (Aoki et al. 1991; Batista et al. 2022; Bräutigam et al. 2017; Bulson 1969; Chen et al. 2020; Godat et al. 2012; Gonçalves and Camotim 2013; Martins et al. 2021; Migita et al. 1992).

Recently, Martins et al. (2021) conducted a comprehensive computational study on the elastic buckling and post-buckling behaviour, with a particular focus on imperfection sensitivity, of regular convex polygonal cross-sections (RCPS) tubular members subjected to bending. The authors employed a geometrically non-linear analysis using the Generalized Beam Theory (GBT) methodology (Schardt 1994). This rigorous analysis aimed to gain insights into the local, distortional and local-distortional interaction buckling modes in the tubular thin-walled members. The study highlighted a significant correlation between the radius-over-thickness ratio and the ultimate flexural capacity of RCPS beams. According to their findings, establishing a reliable design rule for RCPS elements necessitates careful consideration of the radius-over-thickness ratio, along with a thorough evaluation of the performance of the existing design procedure. However, it is crucial to note that, despite the authors conducting a thorough analysis, their focus was exclusively on the flexural behavior of regular convex polygonal sections. Consequently, there exists a noticeable gap in post-buckling studies for conic polygonal sections.

Travanca and André (2018), Travanca et al. (2013) and Bräutigam et al. (2017) have pointed out that the existing standards are not adequately tailored for the specific analysis of monopoles. For instance, the structural design procedures for steel polygonal conic towers considered by TIA (2018) incorporate design equations for the flexural strength capacity of polygonal cross-sections from 8 up to 18 sides. However, for polygonal sections with a higher number of sides, the standard recommends adopting design equations for tubular circular member (CHS), as depicted in Eq. (1). These procedures account for plastic flexural strength ($M_{pl} = Zf_y$, with Z as the plastic modulus of the section and f_y as

the steel yielding stress) for CHS, associating the buckling mode with the cylindrical shell structure, as described by Timoshenko and Gere (1963). Another limitation in the methodology pertains to the restricted maximum value allowed for the diameter-to-thickness ratio (D/t), specifically set at 300. Nonetheless, this approach appears to be a conservative approach for a 20-sided polygonal cross-section, for the cases where the polygonal cross-section along the height is classified as slender, as briefly discussed by Batista et al. (2022).

$$M_{Rk,CHS} = \begin{cases} Zf_y & \text{for, } \lambda \leq 0.0714 \\ \left(\frac{0.0207}{\lambda} + 1 \right) Sf_y & \text{for, } 0.0714 < \lambda \leq 0.309 \\ \frac{0.330}{\lambda} Sf_y & \text{for, } 0.309 < \lambda \leq 300 \frac{f_y}{E} \end{cases} \quad \text{where } \lambda = \frac{D}{t} \frac{f_y}{E}. \quad (1)$$

According to Batista et al. (2022), for polygonal cross-sections with more than 18 sides and considering High Mast Structures (HMS), 40 to 50-meter-high, the polygonal cross-section might be classified as a thin-walled steel tubular section (due to the necessity of higher diameters in the base of the mast). The design of such thin-walled structural systems commonly relies on Winter-type equations (Winter 1968). Notably, the Direct Strength Method (DSM), proposed by Schafer and Peköz (1998), are Winter-based equations, building upon the original concept introduced by Hancock et al. (1994). The cited methodology is well known for the design of cold-formed steel (CFS) members and is included in the following standards: Brazilian (ABNT 2010), North American (AISI 2016) and Australian/New Zealand (AS/NZS 2018). Eqs. (2) and (3) illustrates the DSM applied to assess the flexural capacity, specifically addressing the ultimate limit states (ULS) of local ($M_{Rk,DSM,L}$) and distortional ($M_{Rk,DSM,D}$) buckling.

$$M_{Rk,DSM,L} = \begin{cases} Sf_y & \text{for, } \lambda_L \leq 0.776 \\ \left(1 - \frac{0.15}{\lambda_L^{0.8}} \right) \frac{Sf_y}{\lambda_L^{0.8}} & \text{for, } \lambda_L > 0.776 \end{cases} \quad \text{where } \lambda_L = \sqrt{\frac{Sf_y}{M_{crL}}}. \quad (2)$$

$$M_{Rk,DSM,D} = \begin{cases} Sf_y & \text{for, } \lambda_D \leq 0.673 \\ \left(1 - \frac{0.22}{\lambda_D} \right) \frac{Sf_y}{\lambda_D} & \text{for, } \lambda_D > 0.673 \end{cases} \quad \text{where } \lambda_D = \sqrt{\frac{Sf_y}{M_{crD}}}. \quad (3)$$

In Eqs. (2) and (3) S is the elastic flexural modulus of the section; f_y is the steel yielding stress; Sf_y is the elastic bending moment M_y of the section; λ_L and λ_D are, respectively, the slenderness factors related to the local and distortional buckling; M_{crL} and M_{crD} are, respectively, the critical bending moments related to the local and distortional buckling¹.

Given the limitations of current design guidelines, even for standardized polygonal sections (i.e., from 8 to 18 sides), it remains challenging to enhance and provide a superior structural solution within the existing guidelines. When faced with specific cases to improve the strength capacity, such as the need for openings or an increase in height, viable methods include: (i) conducting advanced finite element analysis, (ii) exploring alternative analytical methodologies like the DSM, or (iii) performing experimental tests. Based on the cited approaches, three practical solutions emerge for improving the strength resistance: (i) increasing the number of sides in the polygon's cross-section, (ii) enhancement of steel material type and thickness, or (iii) reinforcing the cross-section. The latter proves valuable when openings are necessary, while the former may be beneficial for achieving greater pole height, particularly in cases where limitations exist regarding steel material enhancement. These avenues for improvement have not been thoroughly explored for HMS made of polygonal conical sections, creating a gap that warrants attention through advanced numerical analysis and experimental studies.

Recently, Batista et al. (2022) initially suggested assessing longitudinal folded stiffeners as a strategic approach to improve the overall flexural capacity of slender members². For instance, the use of intermediate stiffeners in plane walls

¹ These critical bending moments can be computed through a linear elastic buckling analysis utilizing a generalized eigenvalue formulation, as exemplified by the FStr software (Lazzari and Batista 2021).

² While it is possible to manufacture the stiffened polygonal pole by cold-forming process, the connection solution using the slip joint alternative would need to be developed in order to make it feasible and practical for the erection procedures (Slocum and Fairbairn 2015).

can be advantageous, especially when applied to specific situations such as a thin-walled stiffened trapezoidal CFS roofing system (Franco and Batista 2017; Lazzari et al. 2019). However, it should be more efficiently considered if the ULS is affected by local and/or distortional buckling and the cross-section is classified as slender ($M_{Rk} / M_y \ll 1.0$).

Motivated by (i) the advantages within the telecommunication industry, (ii) the necessity for a deeper understanding of factors influenced by instability phenomena, and (iii) recognizing limitations in existing design procedures, this investigation is centered on conducting computational analyses on an HMS polygonal conical pole for structural design and performance. The analysis aims to propose practical solutions for enhancing the structural performance of these slender structures, such as reinforcements, for openings and folded stiffeners for flat polygon walls (longitudinal stiffeners). The structural assessment specifically focuses on the effects of wind loads, considering the most commonly reported basic gust wind speed in Brazil. The numerical analyses include: (i) vibration mode analysis, (ii) vibration due to turbulent wind, (iii) parametric elastic buckling analysis, (iv) parametric non-linear finite element analysis considering openings with different edge reinforcements and (v) study of polygonal longitudinally stiffened cross-section based on elastic buckling analysis and DSM-based equations to predict the bending moment strength capacity.

The benchmarked geometry under analysis is a 40 m high monopole, based on a proposed 30 meter in height prototype as shown in Figure 1, where a 5900 mm length bottom module of the prototype connected to the ground level foundation is shown. The geometry of the steel cold-formed cross-section is a 20-sided conical monopole (in the elastic buckling analysis, a variety of side numbers have been assessed) with diameters at the bottom and top respectively of 1450 mm and 300 mm (diameter variation-over-height ratio of 28.75 mm/m). The following variables were considered in the present study: the CFS thickness, the geometry of the openings, the geometry of the edges reinforcement, as well as the type (cross-section) of the folded edge stiffeners.

The present article is organized as follows. Section 2 focuses on wind-induced structural analysis. It includes the determination of equivalent static internal forces at the ultimate limit state and provides insights into the dynamic behavior of the structure under wind turbulence and vortex shedding. Section 3 constitutes the core of the paper, presenting a comprehensive structural analysis, which encompasses three main studies. Subsection 3.1: parametric elastic buckling analysis, which explores how the geometry of the polygonal cross-section impacts its behavior, and factors such as different diameters, thicknesses, number of sides and stress distribution types are examined. Subsection 3.2: geometric and material nonlinear finite element analysis, which investigates the conicity effect and the influence of various reinforced opening configurations on the flexural capacity of the structure. Subsection 3.3: DSM-based strength predictions in stiffened polygonal cross-sections, exploring the potential for strengthening these sections by including folded stiffeners. Section 4 provides concluding remarks, summarizing the key findings and implications of the study.

2 WIND-INDUCED STRUCTURAL BEHAVIOR

2.1 Numerical model and vibration mode analysis

The current analysis considers an isolated module panel thicknesses of 6.35 mm up to 18 m above the ground level and 4.75 mm for all others (additional information is included in Section 1). A 3D numerical stick model has been developed, taking into consideration all the masses (of the structure and attachments) and details affecting the structural stiffness, in order to find the global vibration modes and associated frequencies. Soil-foundation-structure interaction is considered by using Terzaghi springs (Terzaghi 1955) to represent soil action and determine the rotational stiffness of the shallow foundation on hard clay soils. At the base of the numerical model, the foundation is represented by an infinitely rigid frame member attached to a moment spring. A slip joint type connection between modules is introduced every 6 m between the mast steel modules. The overlap length is determined by applying a safety criterion to the design hoop tensile stress due to vertical load and overturning moment at each joint. Frame members with thicknesses of both upper and lower modules are inserted into the numerical model to represent the connection of each slip surface. The damping ratio of the structure is set to 1% (ABNT 1988) while the aerodynamic damping, being a minor favorable effect in this case, is neglected. Finally, groups of antennas are considered, according with real conditions described by the telecommunication company and described as follows, for two heights above ground: (i) level 35 m, 50 cm from the pole surface: $3 \times (1.95 \times 0.4 \text{ m})$, $3 \times (0.36 \times 0.26 \text{ m})$, $1 \times (\phi 0.6 \text{ m})$; (ii) level 40 m, fixed to the guardrails of the upper platform: $12 \times (1.96 \times 0.25 \text{ m})$ and $12 \times (0.36 \times 0.26 \text{ m})$.

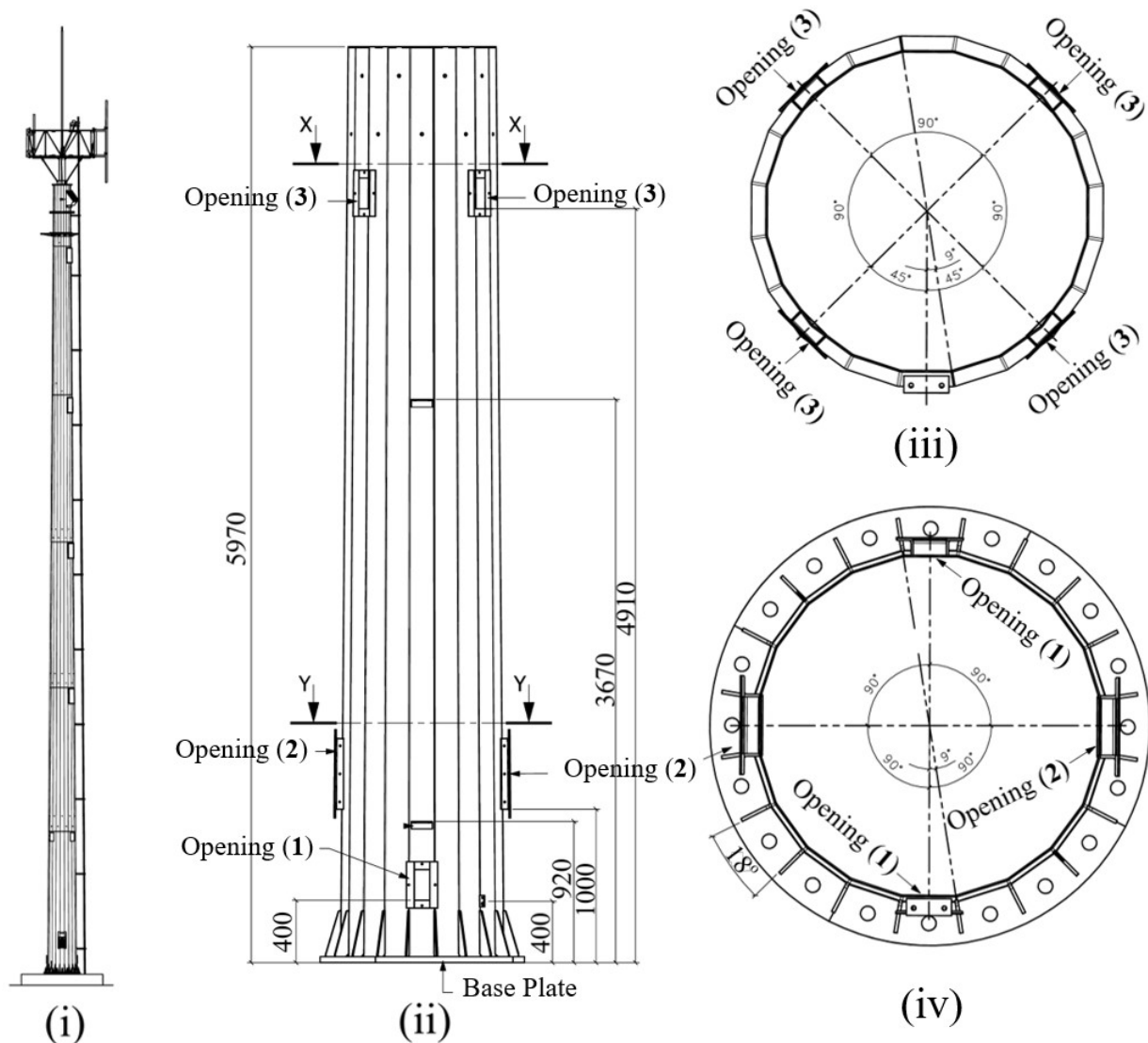


Figure 1 Geometry of the reference 30 m high, 20-sided conic steel cold-formed pole for antennas support: (i) full scale prototype, (ii) bottom (base) at ground level, (iii) section X-X and (iv) section Y-Y (units: millimeters).

The following frequencies were obtained from the vibration mode analysis of the 3D numerical stick model, respectively associated to the pairs of bending mode shapes in xz and yz planes illustrated in Figure 2: 0.52Hz , 1.86Hz and 4.55Hz . The fundamental torsional mode frequency is equal to 5.00Hz .

2.2 Vibration due to turbulent wind

The dynamic analysis of the structure under turbulent wind action is conducted in the frequency domain using the discrete model method prescribed by the Brazilian standard (ABNT 1988) and reviewed by Santos (2018) and Santos et al. (2018), which is based on the classical Davenport (1967) method. The maximum generalized displacement associated to each vibration mode is calculated as the sum of the mean and the maximum fluctuating responses, with the latter being equal to the product of the standard deviation of the fluctuating displacement and the peak factor. The equivalent wind forces are then calculated and applied statically to the numerical model to reproduce the dynamic peak response.

For the ultimate limit state condition, the basic wind speed is taken to be equal to 30m/s , 35m/s , 40m/s and 45m/s at 10m above ground level in a flat and open terrain, averaged within 3s time interval. For these values, Reynolds number (Re) varies in the range from 1.2×10^6 to 1.7×10^6 at the middle height of the upper third of the structure. Below that level, Re increases up to 3.7×10^6 . According to James (1976) and Szalay (1989), who performed wind-tunnel tests on polygonal sections of up to 16 sides for Re below $1,0 \times 10^6$, the drag coefficient of polygonal sections is influenced not only by Re and surface roughness but also by factors such as the corner radius and whether the wind direction points to a corner or not. In a Computational Fluid Dynamics (CFD) study by Tang et al. (2013), a drag coefficient of approximately

0.7 was determined for a 20-sided polygonal cross-section when the wind direction was towards a corner, with a Re of 3.2×10^6 . It is noteworthy that the study also concluded that a cylinder with the same Re achieved a drag coefficient of 0.42. Eurocode 1, Part 4-2005 (CEN 2005) provides the value of 0.70 for the drag coefficient of octadecagon sections with smooth surface and rounded corners subjected to low turbulence flow with Re in the range 2.1×10^5 to 1.2×10^6 . Considering that for higher Re , the drag coefficient tends to increase, and due to the numerous uncertainties associated with determining the drag coefficient, the authors have adopted a conservative value of 0.80. Regarding the antennas' drag coefficients, the following values are adopted in accordance with Brazilian design practice (TELEBRÁS S/A. 1997): 1.2 for rectangular and 1.6 for circular shapes. The antennas mounted at level 40 m (80% of total area) are not subjected to interference effects while these effects were neglected for the antennas at level 35 m by using the superposition method in estimating wind loading.

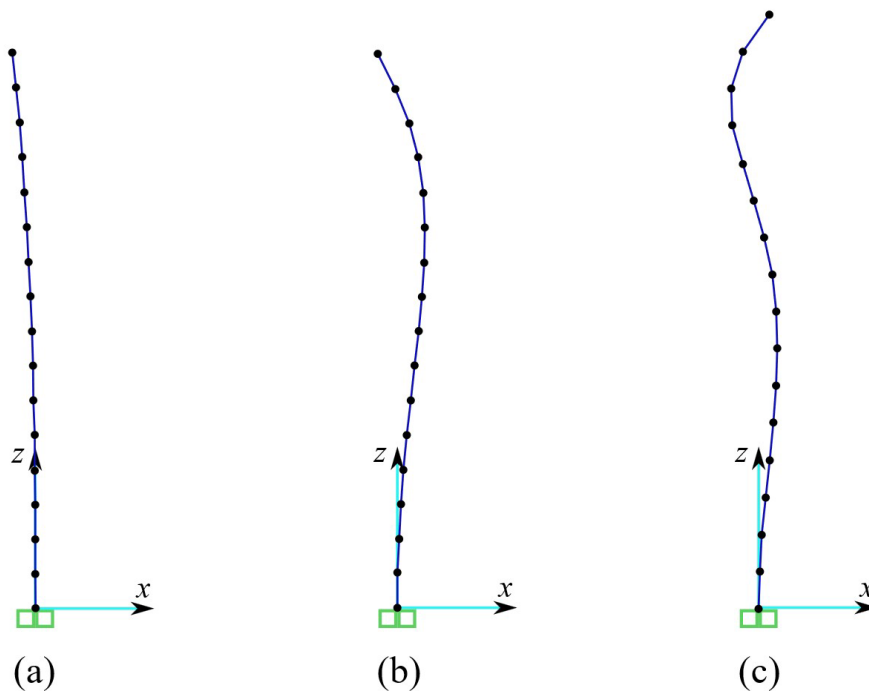


Figure 2 Bending mode shapes in orthogonal vertical planes and associated frequencies: (a) 0.53Hz, (b) 1.86Hz and (c) 4.55Hz.

The bending moment diagram of the pole due to the equivalent drag forces derived from the dynamic analysis considering the first bending mode, for each basic wind speed (V_0) is illustrated in Figure 3. The bending moment is given as a resultant value by combining the along-wind response with the transverse one due to lateral turbulence, estimated as one third of the along-wind fluctuating response (ABNT 1988), on the basis of the relation between turbulence intensities in lateral and longitudinal directions and in the lack of correlation between the wind velocity fluctuations in these two directions. It was found that the drag forces at the antennas are responsible for 65% of the total computed bending moment. Figure 3 gives the design bending moment M_{Sd} due to the factored wind loads. The factored load combination for acting loads, as specified by the Brazilian code (ABNT 2024), is $1.25D+1.4W$, where D represents the dead load of the pole's self-weight and W represents the wind load. The dead load is neglected due to its insignificant effect on the load combination (less than 2%).

The serviceability analyses are conducted to ensure that the antennas do not experience improper behavior or excessive noise due to vibration that may exceed public comfort criteria. Using a 1-year return period (as frequently done for buildings), the peak displacement is estimated to be 0.6m .

The vortex-shedding critical wind velocities were estimated on the basis of Strouhal number equal to 0.18 as for a circular section according to Eurocode 1, Part 4-2005 (CEN 2005): 1.4 m/s , 7.8 m/s and 13.2 m/s respectively for the three bending vibration modes shown in Figure 2. In addition, for the first bending vibration mode, the flow is classified as subcritical, with a Reynolds number of 4.8×10^4 , while for the third and fifty modes, the flow is supercritical, with a Reynolds number of 4×10^5 and 4.8×10^5 , respectively. Applying Ruschewigh method (CEN 2005) resulted in very low vibration displacement amplitudes, equal to 6.7, 6.9 and 2.5 mm respectively for the 1st, 3rd and 5rd modes, coming to the conclusion that the effects of vortex-shedding are not significant in the present case.

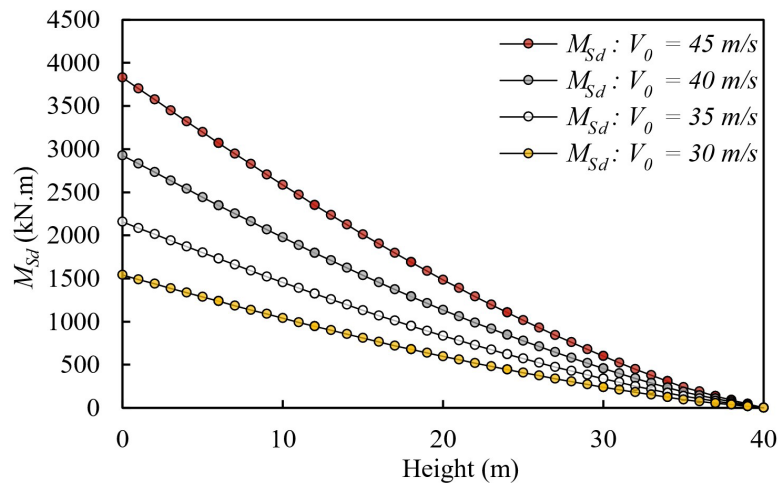


Figure 3 Equivalent static bending moment M_{Sd} due to factored wind loads with basic gust wind speed (V_0) of 30m/s, 35m/s, 40m/s and 45m/s, considering a 20-sided polygonal conic pole, 40-meter-high, bottom diameter of 1450mm and top diameter of 300mm and steel plate with $t = 6.35$ mm and $f_y = 350$ MPa.

3 STRUCTURAL ANALYSIS

3.1 Parametric elastic buckling analysis with prismatic geometry

The elastic buckling analysis is conducted using the *FStr* software (Lazzari and Batista 2021). The cited software, developed at COPPE Federal University of Rio de Janeiro, is a user-friendly computational tool with finite strip method-based formulation. The software conducts an elastic buckling analysis for prismatic structural elements with open and hollow cross-sections. It facilitates the identification of the signature curve, depicting the relationship between buckling stress and member length. Additionally, the software enables the visualization of critical buckling shapes through 2D and 3D images, aided by an intuitive graphical user interface. It is well known that the main advantage of the finite strip method (FSM) formulation (compared to a classical finite element formulation) is to reduce the structure's degrees of freedom, in order to acquire a better performance and time consumption (Cheung 1976; Hancock and Pham 2022; Lazzari 2020; Li 2016; Li et al. 2014), however the method is limited to prismatic elements. A more comprehensive verification of the software, utilizing established methodologies, can be found in the works of Lazzari (Lazzari and Batista 2021; Lazzari 2020).

In the current buckling sensitivity analysis, the parameters under investigation include: (i) the diameter (D) of the polygonal cross-section, measured along the midline of the wall between opposed vertices, varying from 300 to 1450 mm (typical for a 40 m high polygonal monopole with a conicity of 28.75 mm/m), (ii) the thickness (t), and (iii) the number of polygonal sides. It is important to mention that the first step of the buckling analysis was performed with FSM-based solution for prismatic cross-section, and the results were compared with the FEM analysis, revealing accurate results. The effect of the conicity was obtained with the FEM model, as presented later (subsection 3.2.1).

The *FStr*-based elastic buckling analysis was configured to accommodate the following conditions: (i) a regular prismatic polygonal tubular section (conicity not applied in this phase of the study), discretized with at least 2 internal nodal lines for each flat face of the polygon, (ii) CFS material characterized by a Young modulus (E) of 200 GPa, Poisson ratio (ν) of 0.3, and shear modulus (G) of 76.92 GPa, (iii) initial loading in the form of a linear forces distribution simulating a pure bending condition, (iv) simply supported end boundary condition, (v) one term of half-wave, (vi) varied pole lengths ranging from 10 to 10^6 mm, with 100 intermediate values in logarithmic scale, and (vii) a linear elastic numerical solution based on the FSM employing trigonometric longitudinal functions.

Figure 4 depicts the signature curves (i.e., one term of half-wave) and critical buckling modes (both in 2D and 3D) for a 20-sided polygonal cross-section. The steel plate thickness (t) is maintained at 6.35 mm, resulting in a D/t ratio ranging from 47 to 228. Additionally, the *FStr* elastic buckling analysis is compared with the results from the *GBTul* software (Bebiano et al. 2018) for D/t=228. *GBTul* employs a different methodology that evolves the Generalized Beam Theory (Schardt 1994), and the comparison in Figure 4 indicates a close agreement between the two solutions.

To discern the buckling modes concerning the diameter-to-thickness ratio (D/t), a parametric elastic buckling analysis is executed. The analysis consists of varying the diameter-to-thickness ratio D/t, number of sides N_s and initial loading stress distribution. The diameter varies with 41 increments and the thickness is chosen based on realistic manufacturing options (actual available steel plate thickness), from 2.65mm to 6.35mm. The number of sides are selected for the most usual options

for this type of structure, from 16 to 24 sides and only considering even-sided polygons cross-sections. Lastly, the stress distribution is adopted for two different cases: (a) one with the maximum initial stress applied directly to the opposite vertexes of the polygonal cross-section and (b) the other case where opposite plane faces are under the maximum and constant stress distribution. This parametric analysis consists of a total of 246000 generalized eigenvalue problems studied: 100 pole's length, 41 diameters, 6 thickness, 5 number of sides and 2 stress distribution-types. Lastly, the categorization of the present buckling modes relied on visual inspection of the FStr results, as automatic identification of the buckling mode is not available. Illustrations of the elastic buckling modes derived from the FStr analysis are provided in Figure 4 and Figure 5, accompanied by definitions of local (L), distortional (D), and local-distortional (LD) buckling interactions.

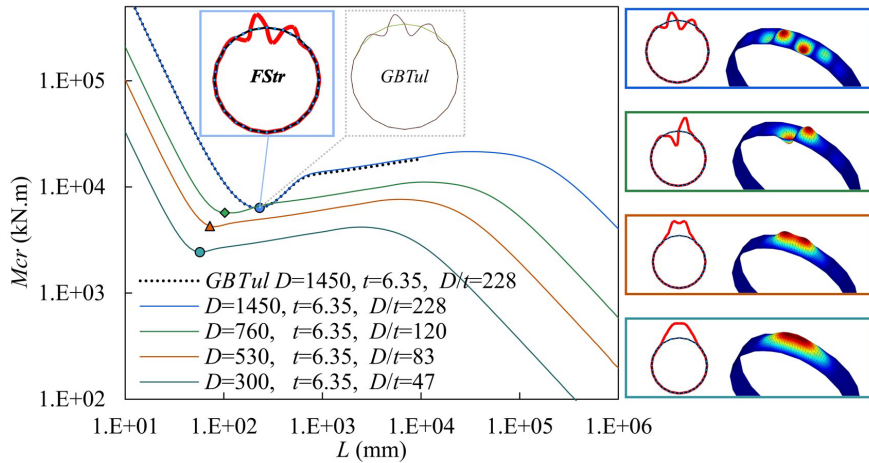


Figure 4 Signature curves given by *FStr* software of a 20-sided polygonal cross-section under pure bending and considering different D/t ratios, compared to the GBT solution, and 2D and 3D illustration of the critical buckling modes produced by *FStr*.

Table 1 presents the FStr results, encompassing the diameter-to-thickness ratio D/t range, for each number of sides, stress distribution type, and elastic buckling mode. The elastic buckling modes include: (i) distortional, (ii) local-distortional, and (iii) local. In Case (ii), the buckling mode incorporates both geometric shapes of local and distortional modes, signifying a distinct interaction between local (L) and distortional (D) buckling.

In order to observe the ranges in Table 1 graphically, Figure 6 illustrates the range transition from (i) distortional to (ii) local-distortional and then to (iii) local buckling mode. The graphs illustrate that the buckling mode can be directly affected by the type of the initial loading applied to the polygonal pole, as well as by the number of sides, in function of the D/t ratio. The buckling mode is classified as local mode where there was no displacement at the vertices of each face. However, if there is such displacement, the buckling mode is classified as distortional mode.

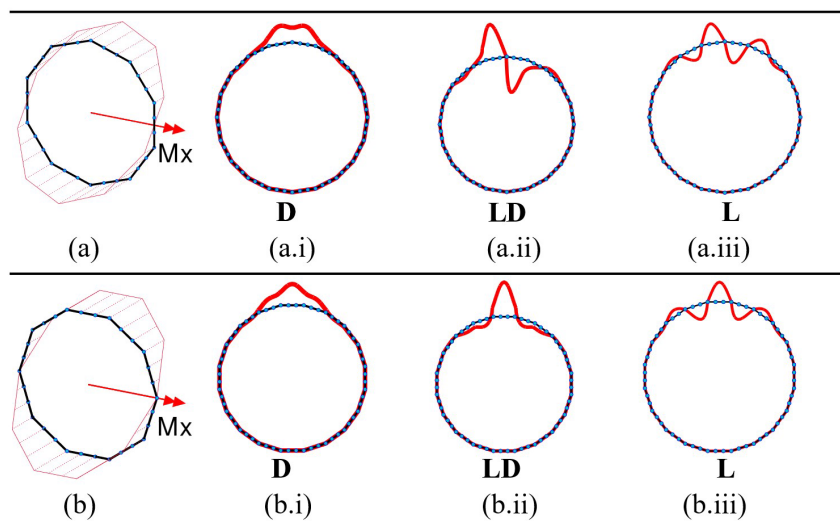


Figure 5 Elastic buckling modes associated to maximum stress distribution at (a) the vertex and at (b) the flat faces, classified as: (i) D, distortional ($D = 415\text{mm}$, $t = 4.75\text{mm}$ and $D/t = 87$), (ii) LD, local-distortional ($D = 472\text{mm}$, $t = 3.75\text{mm}$ and $D/t = 126$) and (iii) L, local buckling mode ($D = 1220\text{mm}$, $t = 3.00\text{mm}$ and $D/t = 407$).

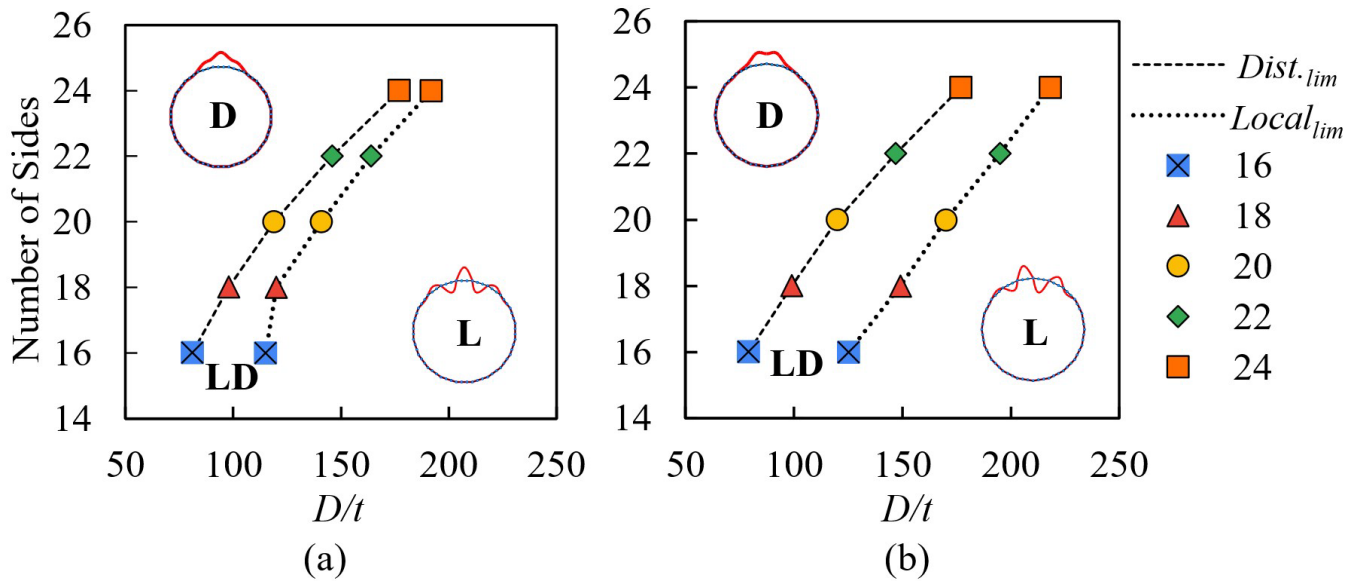


Figure 6 Illustration of the D/t ranges from Table 1 for (i) distortional, (ii) local-distortional and (iii) local buckling mode, considering the maximum initial loading applied: (a) to the flat polygonal face and (b) to the polygonal vertex of the cross-section.

The application of bending moment with maximum stress at the polygonal vertex and the plane polygonal face clearly results in different buckling modes, as illustrated in Figure 5 and Figure 6. Despite that, the critical buckling stress related to the critical bending moment M_{cr} of each loading case is almost identical, with a maximum difference of 0.6% for the cases where the buckling mode is classified as local-distortional. For the cases where the buckling mode is clearly local or distortional, the difference of the critical buckling stress (or M_{cr}) is lower than 0.01%.

Table 1 FStr analysis results for buckling mode classification based on diameter-thickness ratio (D/t), considered number of sides (N_s) of 16, 18, 20, 22 and 24, with maximum stress applied at a flat face and at the vertex.

Stress Distr.	N_s	(i) Distortional (D)	(ii) Local-Distortional (LD)	(iii) Local (L)
Max. at plane face (Figure 5(b))	16	$D/t < 81$	$81 < D/t < 115$	$D/t > 115$
	18	$D/t < 98$	$98 < D/t < 120$	$D/t > 120$
	20	$D/t < 119$	$119 < D/t < 141$	$D/t > 141$
	22	$D/t < 146$	$146 < D/t < 164$	$D/t > 164$
	24	$D/t < 177$	$177 < D/t < 192$	$D/t > 192$
Max. at vertex (Figure 5(a))	16	$D/t < 79$	$79 < D/t < 125$	$D/t > 125$
	18	$D/t < 99$	$99 < D/t < 149$	$D/t > 149$
	20	$D/t < 120$	$120 < D/t < 170$	$D/t > 170$
	22	$D/t < 147$	$147 < D/t < 195$	$D/t > 195$
	24	$D/t < 177$	$177 < D/t < 218$	$D/t > 218$

3.2 Finite element analysis

3.2.1 Description of the computational model

The Finite Element Model (FEM) conducts a material and geometrical nonlinear analysis, utilizing the ANSYS software (ANSYS Inc 2013) through the parametric design language (APDL). Given the limited information on this specific type of modeling in the existing literature, particularly for a conic tubular section under pure bending, several assumptions were made based on the current understanding of computational modeling of CFS. Noteworthy conditions regarding the computational model (Figure 7) include:

- (i) 20-sided polygonal cross-section with diameter variation-over-height ratio (conicity) of 28.75 mm / m (Figure 7(i)).
- (ii) quadrilateral 30x30mm shell finite element, SHELL181 (Figure 7(a), Figure 7(d), Figure 7(e) and Figure 7(h)).

- (iii) bending moment applied as linear loading forces distribution along the polygonal cross-section shape, with the same maximum loading in the polygonal vertex at both end sections (Figure 7(c) and Figure 7(f)).
- (iv) the boundary end condition enables fixed $10 \cdot t$ thick end-plates (t as the pole thickness of the walls), with rotation released only in the direction of the applied bending moment, torsion prevented at both ends and fully restrained displacements in the plane of the end-plates, with axial displacement restrained at a single node located on the neutral plane at one of end-plates (Figure 7(g)).
- (v) nonlinear analysis by the modified Riks method (Crisfield 1981) with mixed displacement and load control.
- (vi) initial geometric imperfection considered as the first critical buckling mode taken from a previous elastic buckling analysis, amplified by 10% of the thickness t (to pass through the bifurcation point the amplitude is selected to be large enough to exclude the trivial solution and small enough to avoid significant influence on the post-buckling mode shape, as proposed by Silvestre (2005)).
- (vii) the material model is based on elastic-perfectly plastic steel model without strain hardening, according to prEN 1993-1-14 (CEN 2022), with $E = 200 \text{ GPa}$ of elastic modulus, Poisson ratio $\nu = 0.30$ and $f_y = 350 \text{ MPa}$ of yield stress.
- (viii) the model neglects the residual stresses of manufacturing and welding (Sabau et al. 2018; Chen et al. 2020), as well as the modification of the mechanical properties of the steel due to cold work in the bent corners (Chen et al. 2020) and the round geometry of the corners (Ellobody and Young 2005; Matsubara and Batista 2023).

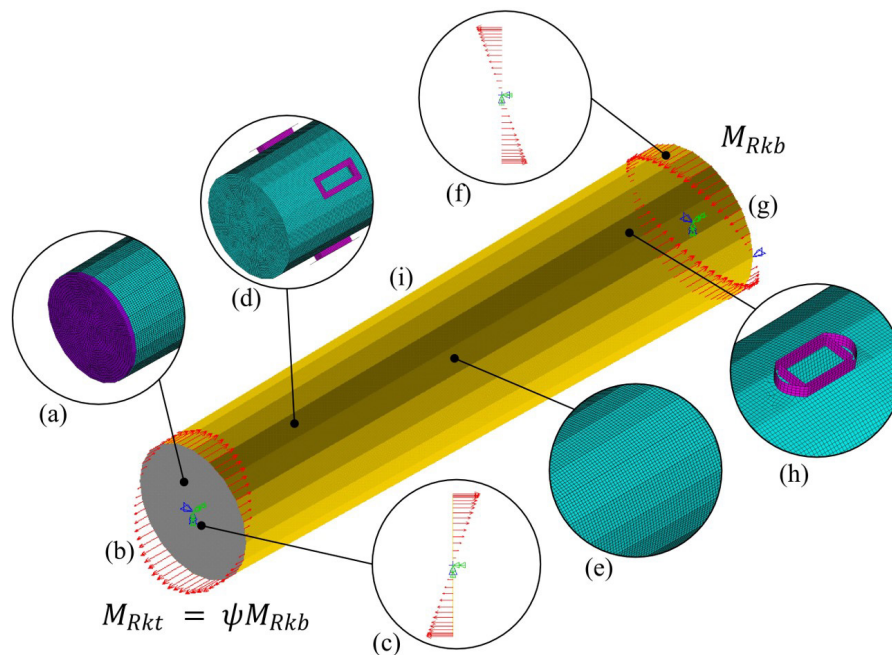


Figure 7 Detail of the finite element model: (a) top fixed-ended end; (b) loading at the top end; (c) loading distribution along the top end; (d) shell element mesh in the openings at the top; (e) mesh at mid-span; (f) loading distribution along the bottom end; (g) loading at the bottom fixed-end; (h) mesh in the opening at the base; (i) 20-sided polygonal conic pole member.

High antenna supports are mainly affected by lateral loads caused by wind-induced behavior, combined with negligible gravity load. In addition, the conical geometry of these structures combined with the lateral wind loading, leads to a problem with typical pure bending condition, with a minor influence of the shear stresses from shear and torsional effect. Building upon the earlier assumption, the applied load at the antenna support is conceptualized as a linear stress distribution at the cross-section ends. This distribution maintains a consistent maximum compressive stress at the extreme fibers of the end sections, resulting in a constant maximum stress diagram along the length of the pole.

Based on the connection elements of the pole, i.e., slip joint and/or flange connection system, the pole is divided into standard modules of 6-meter-length members, which is conservatively analyzed in the present finite element model. Moreover, to facilitate a parametric analysis within a computationally demanding shell finite element model, the present investigation adopts a 6 meter length segment from the bottom end of the pole, with a diameter in the bottom and top equal to 1450 mm and 1278mm (this particular length is deemed representative for finite element analysis based on a prior simplified study (Batista et al. 2022)).

3.2.2 Conicity effect in buckling analysis

In order to verify the FEM with the FSM, the two methodologies are compared (with regards to an elastic buckling analysis). The FSM is limited in terms of describing the element in the longitudinal direction. In this case, only prismatic cross-section can be analyzed. For this case, 4 different models are compared, as illustrated in Figure 8: (i) FSM with prismatic geometry $D = 1364\text{mm}$; (ii) FEM with prismatic geometry $D = 1364\text{mm}$; (iii) FEM with conical geometry ($D_t = 1278\text{mm}, D_b = 1450\text{mm}$) and uniform bending moment (UBM); (iv) FEM with conical geometry ($D_t = 1278\text{mm}, D_b = 1450\text{mm}$) and uniform maximum stress diagram (UMS), as previously described in Figure 7 (all four models have thickness of 2.65mm).

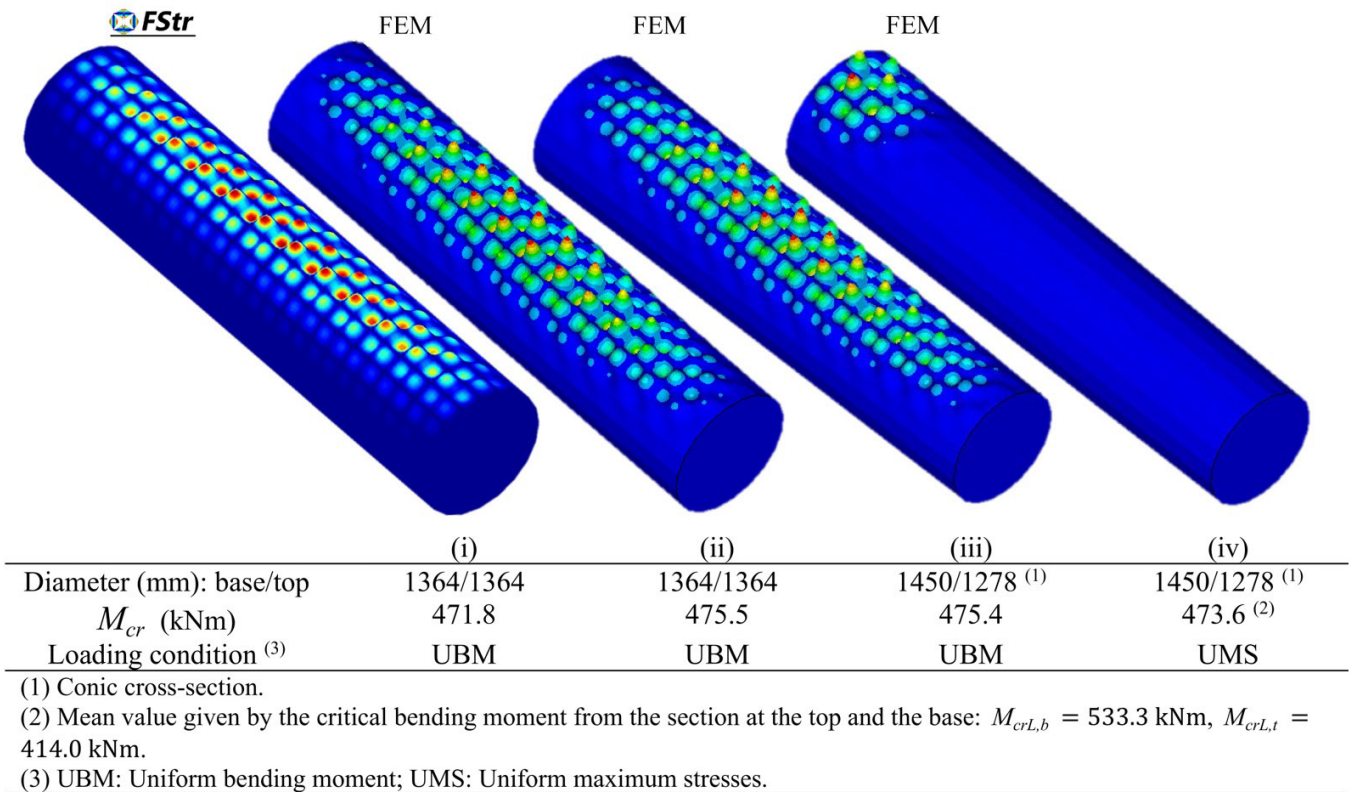


Figure 8 Comparison of the elastic flexural buckling analysis results for a 20-sided polygonal pole with 6 m length, 2.65 mm thickness and considering: (i) uniform bending moment and prismatic geometry in *FStR* software, (ii) uniform bending moment and prismatic geometry in ANSYS, (iii) uniform bending moment and conic geometry in ANSYS and (iv) uniform maximum stresses and conic geometry in ANSYS.

As can be seen in Figure 8, the conicity effect and loading condition (uniform bending moment or uniform maximum stress) shows minor influence of the results of the critical bending moment. However, it changes the critical buckling mode, for the case where uniform maximum stresses (UMS) are applied in both ends. Finally, the structural analysis results presented confirm that the buckling analysis from *FStR*, considering a regular convex geometry (constant diameter), is sufficiently accurate to be deemed suitable for structural analysis and design. This conclusion holds true under the specified geometric conditions, incorporating the pole conicity of 28.75 mm/m .

3.2.3 Nonlinear analysis with reinforced openings

The presence of openings in poles is necessary for equipment and cables facilities to pass through, as well as for maintenance and inspection purposes. However, these openings lead to stress concentration, which weakens the pole's strength under both static and dynamic loading conditions, such as those caused by wind-induced vibration. This condition certainly reduces the pole's overall structural integrity and make it vulnerable to failure.

To assess the impact of openings on a 40-meter height CFS monopole with a thickness of 6.35 mm , the finite element model is used to perform a nonlinear geometric and material analysis. This study only considers the effects of static loading and did not take fatigue into account. In addition, the openings' edges reinforcements are considered in frame condition, which means they are perfectly welded to the steel pole and the welding residual stresses are not considered. The finite element model is described in detail in section 3.2.1 and the mesh around the reinforced openings can be seen

in Figure 7(d), Figure 7(h) and Figure 9. Finally, the bending moment is conditioned to develop maximum stress distribution around the opening (worse case of the wind direction).

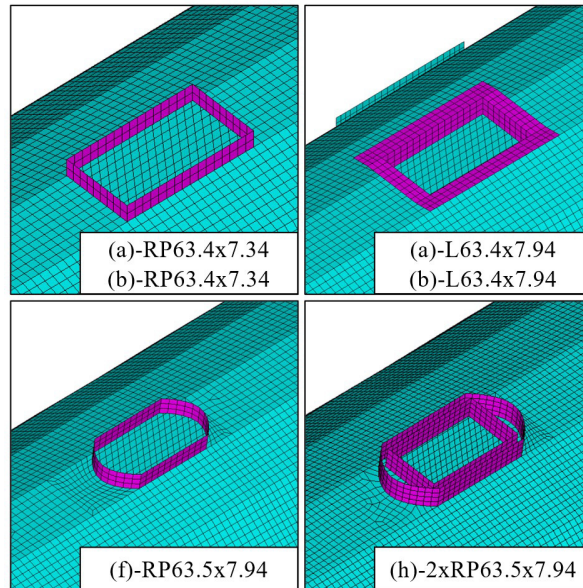


Figure 9 Mesh discretization around the reinforced opening, indicating opening-types according to Figure 10 and reinforcement as described in Table A.1, in **appendix** (L: angle section with equal legs; RP: rectangular steel plate).

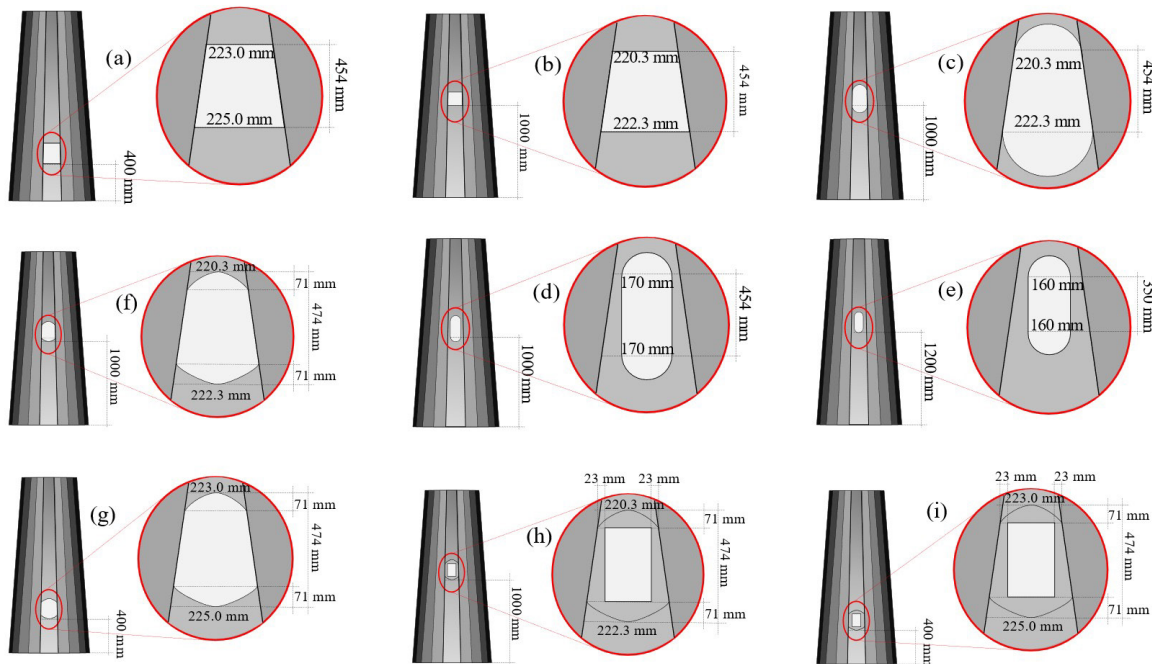


Figure 10 Geometric models for the study of the effect of the openings of 20-sided steel cold-formed polygonal pole with a conicity of 28.75 mm/m , bottom and top diameters respectively of 1450 mm and 1278 mm and thickness of 6.35 mm (image out of scale).

The geometry of the openings considered in the present study are illustrated in Figure 10. The openings (a)-(b), (f)-(g) and (h)-(i), have similar shapes, but they are placed in two different height positions, the same heights as illustrated in Figure 1(ii), for Opening (1) and Opening (2), i.e., openings (a), (g) and (i) are placed 400 mm above the ground level and openings (b), (f) and (h) placed 1000 mm above the ground. Openings (c), (d) and (e) have circular corners but opening (c) is fitted in the plane face of the polygonal cross-section and openings (d) and (e) have a constant width less than the width of the flat face. Opening (e), in particular, has a smaller opening area and is placed higher at 1200 mm .

Table A.1, in appendix, provides the geometric details of reinforcements corresponding to each opening shape depicted in Figure 10. Additionally, it compares the Finite Element (FE) predicted flexural strength (without a safety factor design), denoted as $M_{Rk,FE}$, at the base of the 20-sided pole under different conditions: with and without openings, and with and without reinforcement. Poles with openings and no reinforcement are denoted as "NR," while those with reinforced openings are labeled according to the configurations described in the "Section type" of Table A.1.

The results in Table A.1 (appendix) highlight that the presence of openings weakens the flexural strength of the structure ($M_{Rk,FE}/M_{Rk,FE,NO} < 1$), as expected. Without reinforcement in the opening type (a), the strength is reduced by 45%. However, reinforcements can improve the structural strength reduction from 30% to 3%. The structural strength is mainly affected by the presence of second-order effects due to geometric imperfections around the openings, potentially leading to the plastic collapse around the openings. These deformations and the resulting stress field are depicted in Figure 11 for some of the cases listed in Table A.1.

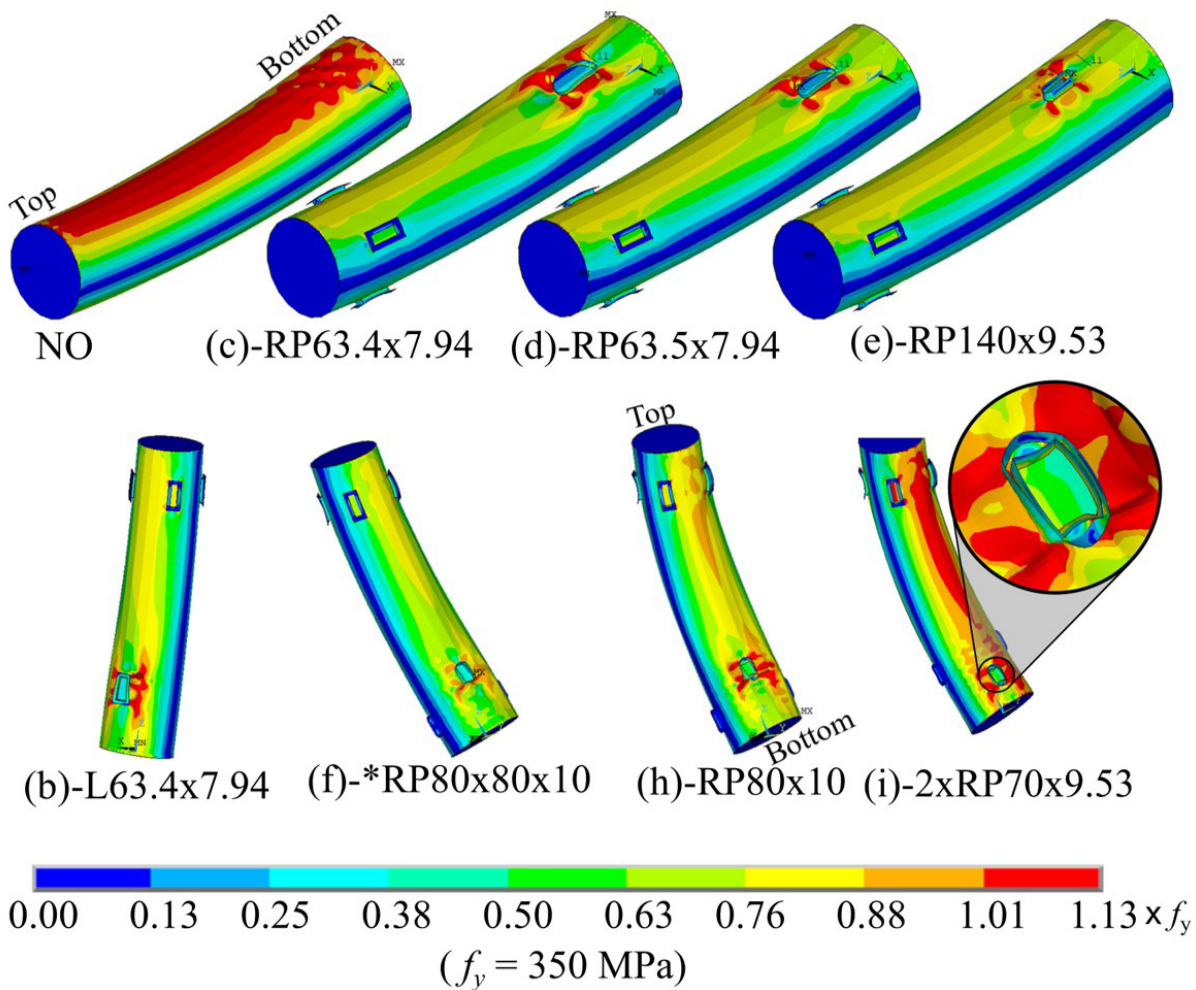


Figure 11 Failure modes of the 20-sided conic pole support with reinforced openings described in Table A.1 (appendix), illustrating the von Mises stress (failure criterion), with amplified deformed shape (* for this specific case, the rectangular plate is applied in both directions, inside and outside of the opening)

One must note in Figure 11 that, for all the cases considered, there are 4 openings next to the top of the 6-meter-long 20-sided pole, which is placed in accordance with the present reference model described in Figure 1. The openings next to the top of the module are reinforced with equal legs angle section L2 1/2x5/16" (63.5 mm width and 7.94 mm thickness). It is important to mention that those openings have negligible influence in the flexural capacity of the pole.

In Figure 12, Figure 13 and Figure 14, the data given in Table A.1 is illustrated. In the horizontal axis, the data is plotted under the ratio A_r / A_p , which is the cross-sectional area of the reinforcing at the centerline of opening (A_r) over the cross-sectional area of the removed element for the opening (A_p). This ratio is related to the total cross-sectional area of the pole and represents the effectiveness of the reinforcement in the opening.

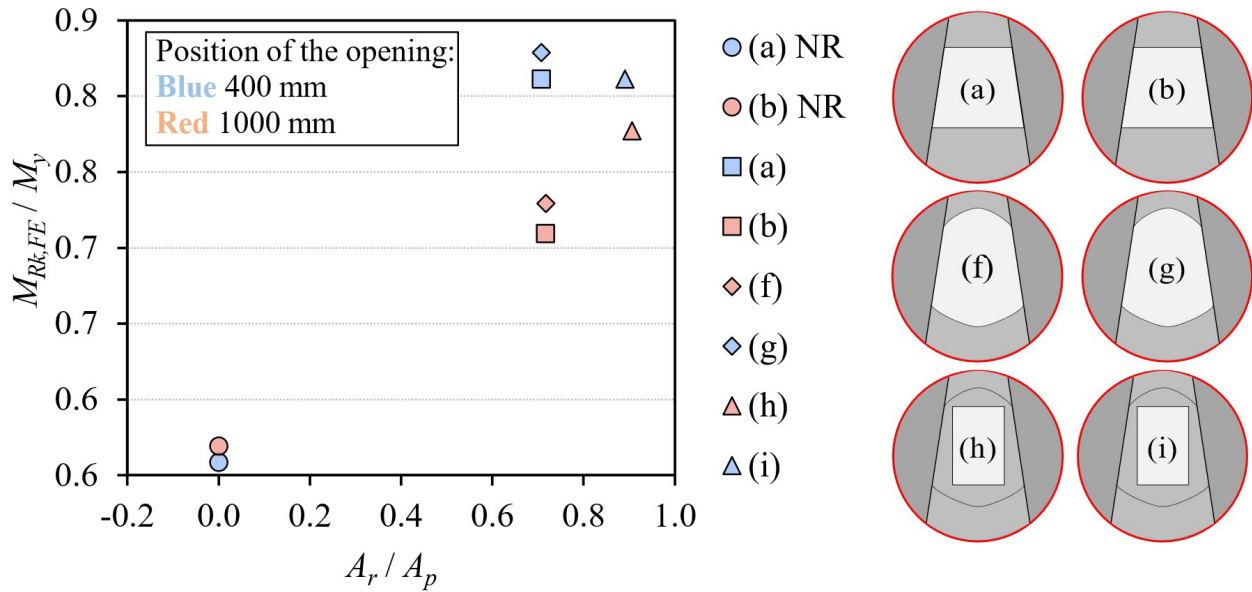


Figure 12 Effect of the position of the opening from the bottom section (see Figure 10) in the bending capacity, considering rectangular plate reinforcement 63.5 mm x 7.94 mm (Blue: position of 400 mm; Red: position of 1000 mm).

Figure 12 addresses the impact of the opening position from the bottom section of the pole in the flexural capacity of the conical pole. The graph shows only the results of openings with NR and with RP 63.5mm × 7.94mm (2 1/2×5/16") reinforcements (a), (b), (f), (g), (h) and (i), given in Figure 10 and Table A.1. The openings 400 mm next to the base (blue points) show higher parametric bending moment capacity $M_{Rk,FE} / M_y$ (except for the NR case, where the difference between the height position of the opening is not relevant, being less than 2%). In addition, the openings (h) and (i) seem to be less efficient, because they combine higher values of A_r / A_p with negligible improvement of resistance related to the height position of the openings ($\Delta M_{Rk,FE} / M_y = 0.03$). This condition may be highlighted if compared with the results of the openings (a)-(b) and (f)-(g) ($\Delta M_{Rk,FE} / M_y = 0.10$).

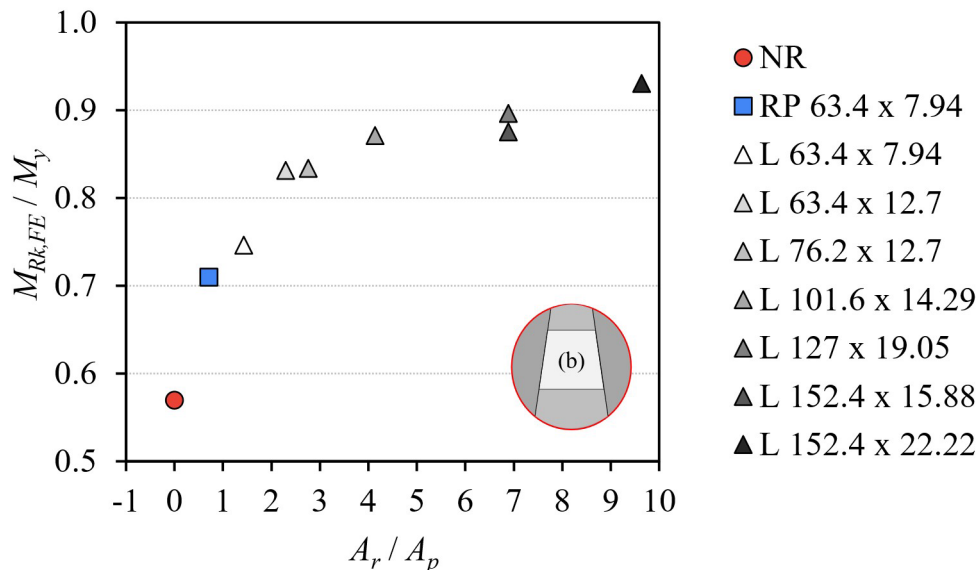


Figure 13 Effect of the cross-section reinforcement in the flexural capacity of the opening (b).

Regarding the influence of the reinforcement cross-section type in the bending moment capacity of the conical pole, Figure 13 addresses the following case: only the opening (b) is considered (Figure 10) with 9 cases analyzed, where the reinforcement cross-section are NR, RP or L-section shape. It is clear to notice that, with more robust reinforcement the opening becomes stiffer, arising both conditions: (i) improving the flexural resistance and (ii) achieving more important stress concentration around the reinforcement. On the other hand, it is important to mention that some of the options

adopted as reinforcement in the present analysis might not be practicable in a real manufacturing condition. In this context, welding procedure must be carefully observed for the case of combining the 6.35mm thickness of the pole with 19.05mm and 22.22mm thickness for the angle sections.

Figure 14 shows the results of all the cases described in Table A.1 in two different perspectives. Figure 14(a) compares the analyzed cases with the equivalent static bending moment at the base of the pole due to wind-induced dynamic behavior (M_{Sd}), given by the structural dynamic analysis, compared to the design predicted finite element flexural strength with a safety factor ($M_{Rd,FE} = M_{Rk,FE} / 1.1$). The equivalent static design bending moment M_{Sd} is given for the most common basic gust wind speed in Brazil (Loredo-Souza et al. 2022): 30m/s, 35m/s, 40m/s and 45m/s. As can it be seen, for basic wind speed of the 30m/s and 35m/s, all the reinforced openings are in the safe region ($M_{Rd,FE} / M_{Sd} > 1.0$). On the other hand, for basic wind speed of 45m/s, none of the proposed cases are safe. Regarding the basic wind speed of 40m/s, only the reinforced openings, (b)-L152.4x22.22 mm and (i)-2xRPx70x9.53 mm, are in the safe margin. In addition, with respect to the opening with no reinforcement ($A_r / A_p = 0$), it is only safe for the case of basic wind speed of 30m/s.

Figure 14(b) displays the results of the parametric flexural capacity $M_{Rk,FE} / M_y$ of each opening illustrated in Figure 10. The results identify each opening performance, with respect to its effectiveness in the flexural capacity. As reported in Figure 13, higher cross-section area of the reinforcement promotes the improvement of the flexural capacity. However, in Figure 14 (b) it is clear to notice that the reinforced opening (i) with double rectangular plates (see detail of opening (i) in Figure 9) has provided the best efficiency, by combining higher bending strength $M_{Rk,FE} / M_y$ with lower A_r / A_p ratio. Also, the option (i)-2xRPx70x9.53 mm has shown safe results even for basic wind speed of 40m/s. One must note that the cited reinforcement option has increased the flexural strength very close to the yielding bending moment ($M_{Rk,FE} / M_y = 0.99$), corresponding to a design ideal condition.

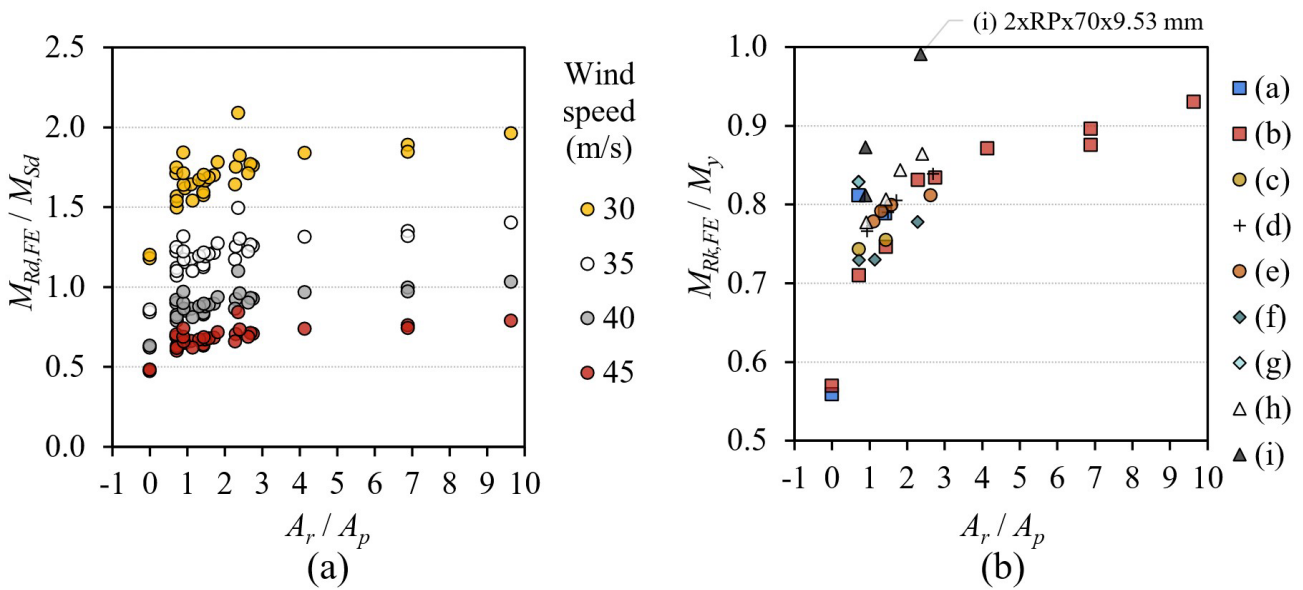
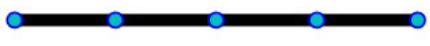


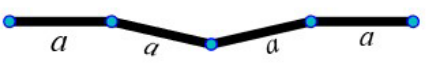





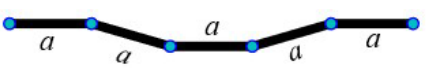


Figure 14 Results of openings with reinforcement described in Table A.1: (a) ratio between the predicted finite element design flexural strength $M_{Rd,FE}$ and the design bending moment M_{Sd} due to factored wind loads given in Figure 3; (b) parametric flexural capacity $M_{Rk,FE} / M_y$ of each opening type illustrated in Figure 10.

3.3 Evaluation of stiffened polygonal thin-walled section

For the present study, several types of folded stiffeners of the polygonal section are analyzed. The objective of the study is to understand the possibility of increasing the strength of a 20-sided polygonal pole, with a prismatic geometry with diameter of 1450 mm (bottom diameter). For this study, the usual commercialized steel coil thickness (t) is considered: 2.65mm, 3.00mm, 3.75mm, 4.25mm, 4.75mm and 6.35mm. Concerning the stiffeners' geometry, 9 types were considered, A to H plus G2 in Figure 15, most of them with a depth of $2 \cdot t$, except for stiffener B with a depth of $4 \cdot t$ (see Figure 15 for general description and Table A.2, in appendix, for more geometry details). The geometry is based on two types of stiffeners: (i) 4-fold (trapezoid) stiffener and (ii) 3-fold (triangle) stiffener. Stiffeners can be strategically applied either along the flat walls or at the vertices of the polygonal cross-section. Also, it was considered that the alternate

distribution of the stiffeners shown in Figure 16(iii) is unable to deal with the local buckling, since the cross-section remains with slender unstiffened faces. Anyway, the vertex stiffener F was taken in alternate condition, as described in Figure 15 and Table A.2 (10 bent corners of the total of 20 received the vertex stiffener). The description of the geometry parameters of the stiffeners are illustrated in Figure 16(i) for an intermediate 4-fold stiffener and Figure 16(ii) for a vertex 3-fold stiffener. Figure 16(iii) and Figure 16(iv) illustrate examples of intermediate stiffeners in the plane walls of a polygonal cross-section, given by a manufacturer prototype and modeled by the *FStr* software, respectively.

NS		Non-stiffened cross-section
A		Intermediate double 3-fold (triangle) stiffener with $2t$ of depth;
B		Intermediate single 4-fold (trapezoid) stiffener with $4t$ of depth (same area as stiffener A);
C		Intermediate wide single 3-fold stiffener with $2t$ of depth (the 4 flat wall elements have the same width a);
D		Intermediate double 4-fold stiffener with $2t$ of inside depth (same area as stiffener A and B);
E		Intermediate double 4-fold stiffener with $2t$ of outside depth (external stiffener with same area as A, B and D);
F		Alternate vertex* single 3-fold stiffener with constant depth of 41.82 mm (according with a prototype produced by a steel structures manufacturer);
G		Intermediate single 4-fold (trapezoid) stiffener with $2t$ of depth;
G2		Intermediate single 4-fold (trapezoid) stiffener with $2t$ of depth, with maximum stresses applied to the flat faces of the polygonal cross-section (see Figure 5(b));
H		Intermediate wide single 4-fold (trapezoid) stiffener with $2t$ of effective depth (the 5 flat wall elements have all the same width a).

* Alternate vertex means the folded stiffener is applied in half of the folded bent corners: 10 vertex stiffeners for the total of 20 folded corners.

Figure 15 Types of wall folded stiffeners configuration adopted in the present study (dimensions displayed in Table A.2).

The geometric dimensions of the stiffeners presented in Figure 15 (based on the parameters defined in Figure 16(i) and Figure 16(ii)) are shown in Table A.2. The approach of the present study is to understand the influence of the stiffeners in the predicted bending moment strength, by using an alternative analytical approach. To achieve this, $M_{Rk,DSM,L}$ and $M_{Rk,DSM,D}$ are defined by Eq. (2) and Eq. (3), respectively for local and distortional buckling, as an estimative to predict the flexural capacity (where M_{crL} and M_{crD} were computed with the *FStr* software).

The equations mentioned were previously verified by the authors for the unstiffened 20-sided conic polygonal thin-walled section (Batista et al. 2022). The authors demonstrated that Eqs. (2) and (3) provided negligible differences with the results obtained from the FE buckling analysis. On the contrary, Eq. (1), recommended by TIA (2018) for tubular circular members and polygonal cross-sections higher than 18, was shown to be inaccurate for predicting the ultimate flexural capacity of 20-sided thin-walled polygonal sections.

The evaluation of the bending moment strength of the stiffened polygonal cross-sections was accomplished with the initial parameters used for the finite strip analysis with the *FStr* software, following the previous analyses described in section 3.1. In addition, the initial loading applied in the stiffened models is defined with a bending moment with maximum stress at the polygonal vertex (except for the stiffener G2, where the maximum stresses were applied at the plane faces of the polygonal with the stiffener). The previous buckling analyses confirmed that the critical buckling stresses are almost identical (maximum difference of 0.6%), for the two cases considered of initial loading distribution along the polygonal cross-section.

Since stiffened sections may improve the strength capacity of the thin-walled 20-sided polygonal cross-section affected by local buckling, it is inevitable that the distortional buckling replaces the local buckling as the cross-section critical buckling mode, leading to a distortional buckling mode failure. In addition, one may observe that local-distortional buckling interactions may develop, for the cases where local and distortional critical bending moments M_{crL} and M_{crD} are relatively close. The local-distortional buckling mode interaction of CFS members is still an open subject of investigation, although recent studies presented satisfactory results for the case of open CFS members (Matsubara et al. 2019; Matsubara and Batista 2023). In the present study only the design procedure of Eq. (2) and Eq. (3) are considered, following the current design methods included in recognized codes and standards (AISI 2016; ABNT 2010; AS/NZS 2018).

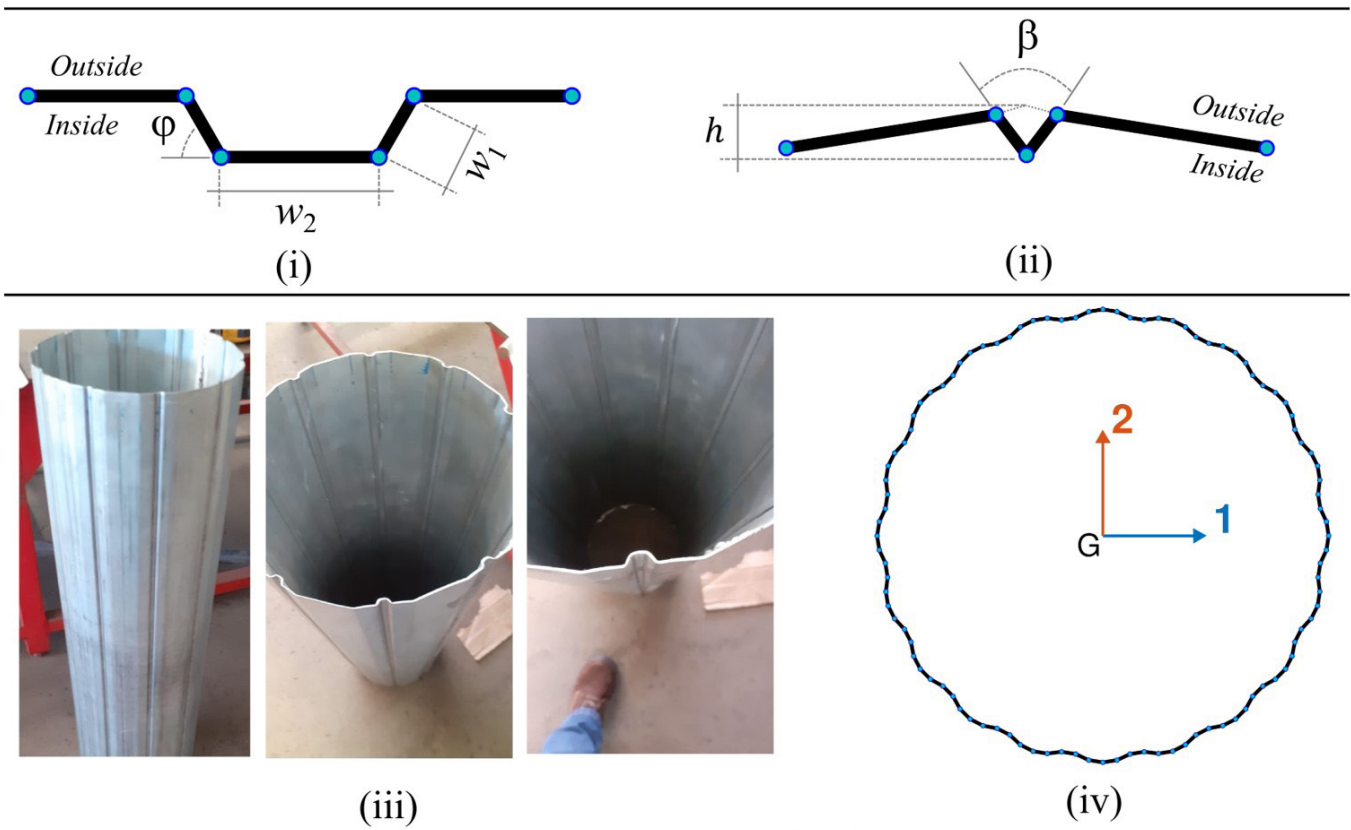


Figure 16 Folded stiffeners of cold-formed polygonal cross-sections: (i) single 4-fold (trapezoid) intermediate stiffener dimensions; (ii) single 3-fold (triangle) vertex stiffener dimensions; (iii) example of an alternate trapezoid stiffener in a 20-sided polygonal cross-section prototype; (iv) example of a 20-sided polygonal cross-section with a wide trapezoid stiffener (type H in Figure 15) modeled for buckling analysis by *FStr* software.

Table A.2 and Figure 17 show the results of the nine cases of stiffeners A to H and G2 (Figure 15), considering the cited thickness 2.65 to 6.35 mm. Figure 17(a) displays the ratio $M_{Rk,DSM} / M_y$ of the DSM predicted flexural strength

$M_{Rk,DSM}$ obtained with the minimum between Eq. (2) and Eq. (3), $\min(M_{Rk,DSM,L}, M_{Rk,DSM,D})$, over the elastic yielding bending moment M_y . One may observe that the non-stiffened (NS) 20-sided polygonal cross-section has mostly the lower strength ratio. Indeed, by applying stiffeners it is possible to increase the strength capacity ratio in almost all the cases, with exception of the stiffener type A, for which negligible strength improvement is found. However, for the stiffeners B, G, G2 and H (G and G2 are almost coincident in the graph) the improvement of the flexural capacity can be noticed. The same conclusion may be obtained from Figure 17(b). These most efficient stiffening types are based on trapezoid intermediate stiffeners with effective depth of $2 \cdot t$ (G, G2 and H) or $4t$ (B), confirming the conclusions for stiffened trapezoidal CFS self-supporting roof systems (Franco and Batista 2017). Finally, stiffener types C, D and E show acceptable strength improvement and the vertex type F confirmed its inappropriate structural performance since it does not offer efficacy for the local buckling.

Regarding the critical buckling mode, all the results of the 1450 mm diameter stiffened 20-sided polygonal members included in Table A.2 and Figure 17 developed distortional buckling. These results contrast with those of the unstiffened condition (NS), for which local buckling is the critical buckling mode, thus proving the efficacy of all the adopted stiffening types.

Finally, it must be observed that the bending strength $M_{Rk,DSM}$ was computed with Eq. (2) and Eq. (3), which is a DSM-based calibrated solution for open CFS sections (i.e., lipped channel, hat, zed, rack sections). Even though the DSM-based procedure has been checked in a previous study (Batista et al. 2022), it is premature to say that Eq. (3) could be used for conical polygonal hollow sections with stiffeners. In the previous paper (Batista et al. 2022), the effectiveness of the DSM-based equations was studied for conical polygonal hollow sections with plane walls, i.e., without stiffeners and it was concluded that the Eq. (2) (local buckling effect) could be used as a design procedure. In this matter, Eq. (3) could not be fully acceptable since it was not calibrated for the case of conical polygonal cross-sections with intermediate stiffeners. The inclusion of such folded stiffeners introduces complexities, and the Eq. (3) may not adequately account for the diverse distortional buckling effects, especially when multiple distortional modes could arise. This aspect should be checked in future investigations, including FEM and experimental tests involving stiffened CFS conical polygonal members under uniform bending loading.

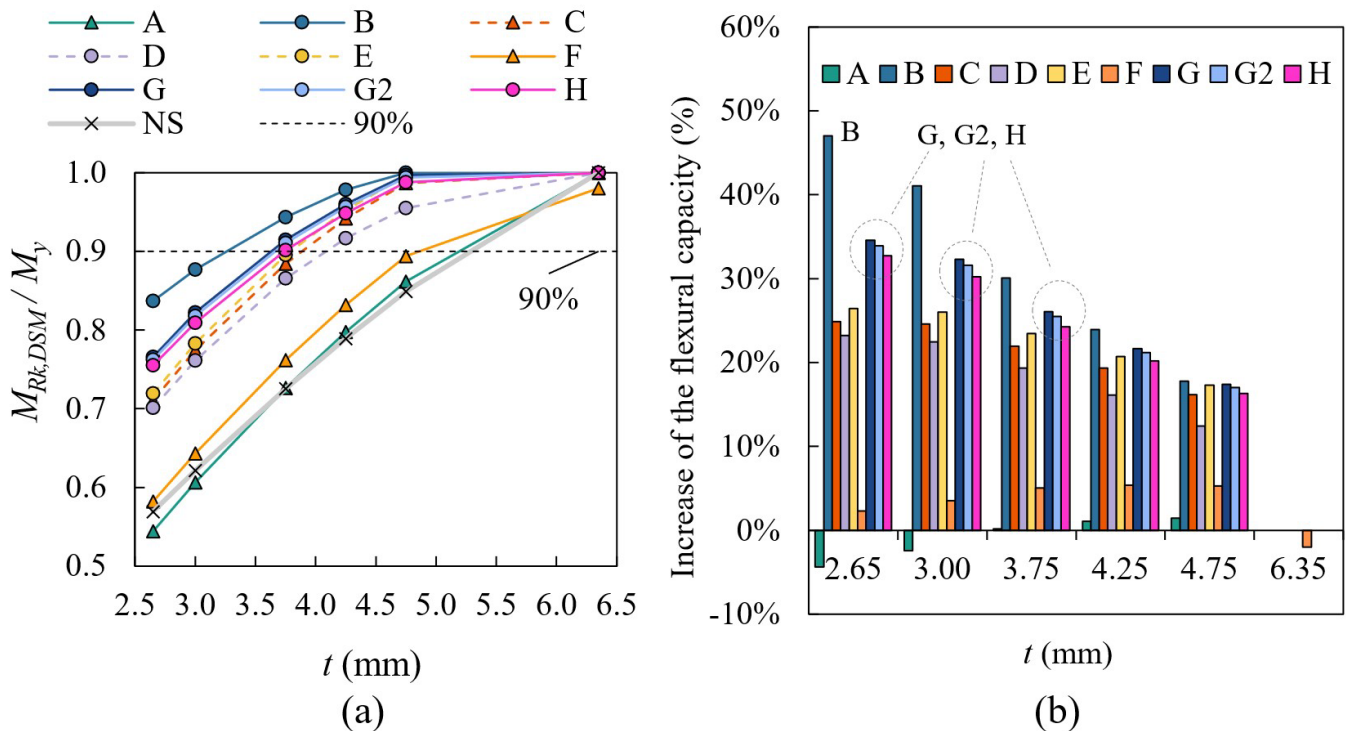


Figure 17 DSM flexural capacity prediction with intermediate and vertex stiffeners, compared to the non-stiffened (NS) 20-sided polygonal cross-section, with prismatic geometry $D=1450$ mm and thickness from 2.65 mm to 6.35 mm : (a) $M_{Rk,DSM} / M_y$, (b) increase of the flexural capacity in comparison with the NS cross-section.

4 CONCLUDING REMARKS

The outcomes of the current investigation suggest that an enhanced solution for a 20-sided conic CFS polygonal pole is structurally feasible for supporting telecom antennas up to 40 meters above the ground. The study incorporated considerations of wind-induced behavior, structural stability analysis, the assessment of reinforced openings, and improved stiffened thin-walled polygonal cross-sections. The study provided structural improvements and delved into the phenomena of buckling. Key conclusions drawn from the present research can be summarized as follows:

- (i) Through the dynamic structural analysis, fundamental information has been obtained about the internal forces caused by the dynamic behavior and wind turbulence. In addition to the identification of the bending modes as the most common natural vibration modes of the studied pole, the vibrations caused by turbulent wind were adopted to compute the distribution of the equivalent static bending moment along the pole's length, which can be used for engineering design purposes, taking into account the typical wind speeds in Brazil. Furthermore, it was concluded that the vortex-shedding vibration phenomenon has a minimal impact on these types of pole structures (at least for the geometric properties considered in the present investigation).
- (ii) The elastic buckling analysis conducted using the *FStr* software has successfully identified critical buckling modes, including local (**L**), distortional (**D**), and local-distortional (**LD**) buckling interactions. Notably, this identification has revealed a significant relationship between these modes and both the number of sides and the D/t (diameter-to-thickness) ratio. Consequently, for a reliable design procedure, it becomes imperative to consider both parameters to accurately predict the strength of polygonal monopoles.
- (iii) Indeed, the elastic critical buckling analysis holds a fundamental role in the design of such slender structures. It is essential to highlight that, following the principles of the DSM (as expressed in Eq. (2) and Eq. (3)), it facilitates the examination of local and distortional buckling interactions as distinct and uncoupled phenomena. However, for the case of clear local-distortional buckling mode (the buckling mode must be classified by observing the shape of the deformation displayed by the computational program *FStr*, actually the solution of a generalized eigenvalue problem) it would be expected to apply a structural strength solution other than Eq. (2) and Eq. (3) (each one devoted to single local or distortional buckling modes, respectively). Anyway, as this solution is only available at the research step by now, the authors decided to keep the design prescriptions consolidated in internationally recognized codes and standards.
- (iv) The FEM employed in this study facilitated an in-depth examination of the effects of conicity and openings, particularly in the bottom region of the conic pole. Verification of the FEM was conducted using the FSM and comparison with prismatic and conic geometries. Minimal differences were observed across all models, especially for the 6-meter-long benchmark structural model. The FEM has confirmed the adequacy of the FSM when employing prismatic geometry. This verification indicates that FSM, with a prismatic approach, is sufficiently accurate for conducting precise structural analyses and designing geometries with a conicity of 28.75 mm/m. Moreover, various configurations, including geometric variations of openings combined with steel angles and rectangular plate elements welded around the edges, were tested. The results, focusing on the bending moment capacity of the pole member in relation to elastic-plastic failure configurations, allowed the identification of optimal solutions crucial for structural design considerations.
- (v) The parametric study concerning the effect of the reinforcement of the opening has demonstrated that the inclusion of openings without reinforcement leads to a significant reduction in the flexural capacity ($M_{Rk,FE} / M_y$), amounting to nearly 50%. However, with the adoption of reinforcements, the flexural capacity can be enhanced, reaching levels ranging from 70% to as high as 97% of the elastic bending moment (M_y).
- (vi) In the context of verifying the design bending moment resulting from factored wind loads based on typical wind speeds in Brazil, the study has yielded significant insights. It has been established that for wind speeds of 30 m/s , 35 m/s , and 40 m/s , it is feasible to design with adequate safety margins using some of the suggested reinforcements. However, when faced with a basic wind speed of 45 m/s , none of the proposed reinforcement solutions proved sufficient to strengthen the 40-meter-high polygonal conical pole to meet the required safety standards.
- (vii) Stiffened polygonal cross-sections were evaluated, using finite strip method software to obtain: (i) the critical buckling bending moment and (ii) the bending moment strength predicted by the DSM-based equations Eq. (2) and Eq. (3). Typically, the local mode was only critical for the case of the unstiffened polygonal section (NS), while the distortional mode was predominant for the others. The consideration of different configurations of stiffened sections, including trapezoid (4 folds) and triangular (3 folds)

intermediate stiffeners as described in Figure 15 and Table A.2, changed the buckling mode from local to distortional. Moreover, the results of the buckling analysis indicated the trapezoid stiffeners offer better results if compared with the triangular shape. In addition, it was shown that only intermediate stiffeners demonstrated effectiveness for the local buckling and that the vertex option may be disregarded.

While fatigue was not explicitly addressed in this study, the authors acknowledge its significance in structural design. This includes considerations for welded details around the openings, the connection between the pole and the end plate connected to the concrete foundation block, as well as the flange bolted connections between pole members during erection.

Wind tunnel tests would bring additional information of the wind forces over the structure, allowing refinement of the structural design fundamentals and comparison with the adopted drag coefficient of the particular geometry of the poles. In addition, the actual structural performance of the polygonal steel member could be obtained with the help of full-scale experimental tests, taking into consideration a setup of a representative length of the pole under bending (according with the experimental facilities of the laboratory) and allowing refining the definition of the collapse configuration and its correspondence with the structural strength equations considered in the present investigation. The authors expect a possible extension of the present investigation in both directions (wind tunnel and structural tests) in the near future.

The results of this study provide theoretical engineering basis for improving the structural design of polygonal conical monopoles used to support telecom antennas. The presented results and findings are intended as a contribution to guidelines for the development of more effective design of such structures.

Acknowledgements

The authors wish to express their gratitude to BrasilSat Harald S/A for collaborating with the COPPE research group, which made this study possible. The second author is grateful for the Foundation for Science and Technology's support through funding UIDB/04625/2020 (<https://doi.org/10.54499/UIDB/04625/2020>) from the research unit CERIS. The third author also wants to thank the Conselho Nacional de Desenvolvimento Científico e Tecnológico (CNPq) research agency for providing a grant (# 141287/2019-5) for this work.

Author's Contributions: Conceptualization, EM Batista; Methodology, EM Batista, JA Lazzari, GY Matsubara, MS Pfeil and RN Elias; Software, JA Lazzari, GY Matsubara, MS Pfeil and RN Elias; Investigation, JA Lazzari, GY Matsubara, MS Pfeil and RN Elias; Writing - original draft, JA Lazzari and GY Matsubara; Writing - review & editing, EM Batista, JA Lazzari, GY Matsubara, MS Pfeil and RN Elias; Funding acquisition, EM Batista and MS Pfeil; Resources, EM Batista; Supervision, EM Batista.

Data Availability Statement: All data, models, or code that support the findings of this study are available from the corresponding author upon reasonable request. Supplementary material related to the FStr software can be found online at <http://dx.doi.org/10.17632/3hpfxc642.2>, <https://joaoadelazzari.github.io/FStr/> and <https://sites.google.com/coc.ufrj.br/fstr> .

Editor: Pablo Andrés Muñoz Rojas

References

- ABNT (Associação Brasileira de Normas Técnicas) (1988). NBR 6123:1988 - Building Construction - Bases for Design of Structures - Wind Loads – Procedure (in Portuguese: Forças Devidas ao Vento em Edificações), Rio de Janeiro, Brazil.
- ABNT (Associação Brasileira de Normas Técnicas) (2024). NBR 8800:2024 – Design of Steel and Composite Structures for Buildings (in Portuguese: Projeto de Estruturas de Aço e de Estruturas Mistas de Aço e Concreto de Edificações), Rio de Janeiro, Brazil.
- ABNT (Associação Brasileira de Normas Técnicas) (2010). NBR 14762:2010 - Design of Cold-Formed Steel Structures (in Portuguese: Dimensionamento de Estruturas de Aço Constituídas por Perfis Formados a Frio), Rio de Janeiro, Brazil.

- AISI (American Iron and Steel Institute) (2016). S100-16 - North American Specification for the Design of Cold-Formed Steel Structural Members, Arlington, EUA.
- Amponsah, E., S. A. Takyi, M. O. Asibey, and O. Amponsah, (2022). Assessing the level of compliance of telecommunication masts to locational planning standards towards harmonious and orderly city growth, *Cities Health*, 6 (4): 777–790, Routledge, <https://doi.org/10.1080/23748834.2021.1956837>.
- ANSYS Inc. (2013). ANSYS Mechanical APDL Theory Reference, ANSYS Inc. Canonsburg, PA.
- Aoki, T., Y. Migita, and Y. Fukumoto, (1991). Local buckling strength of closed polygon folded section columns, *J Constr Steel Res*, 20 (4): 259–270, Elsevier, [https://doi.org/10.1016/0143-974X\(91\)90077-E](https://doi.org/10.1016/0143-974X(91)90077-E).
- AS/NZS (Australian/New Zealand Standard) (2018). AS/NZS 4600 - Cold-Formed Steel Structures, Sydney, Australia.
- Batista, E. de M., J. A. de Lazzari, G. Y. Matsubara, and M. Pfeil, (2022). Structural dynamic and buckling behaviour of steel cold-formed polygonal conic pole for antennas support, *ce/papers*, 5 (4): 151–160. John Wiley & Sons, Ltd., <https://doi.org/10.1002/cepa.1740>.
- Bebiano, R., D. Camotim, and R. Gonçalves, (2018). GBTul 2.0 – A second-generation code for the GBT-based buckling and vibration analysis of thin-walled members, *Thin-Walled Structures*, 124: 235–257, Elsevier, <https://doi.org/10.1016/J.TWS.2017.12.002>.
- Bräutigam, K., Knoedel, P. and Ummenhofer, T., (2017). Plastic behaviour of polygonal hollow sections in bending, *Steel Construction*, 10: 222-226, <https://doi.org/10.1002/stco.201710027>.
- Bulson, P. S., (1969). The strength of thin-walled tubes formed from flat elements, *Int J Mech Sci*, 11 (7): 613–620, Pergamon, [https://doi.org/10.1016/0020-7403\(69\)90060-5](https://doi.org/10.1016/0020-7403(69)90060-5).
- Capello, R., and P. Nijkamp, (1996). Telecommunications technologies and regional development: theoretical considerations and empirical evidence, *The Annals of Regional Science* 30:1, 30 (1): 7–30, Springer, <https://doi.org/10.1007/BF01580535>.
- Cardoni, A., S. L. Borlera, F. Malandrino, and G. P. Cimellaro, (2022). Seismic vulnerability and resilience assessment of urban telecommunication networks, *Sustain Cities Soc*, 77, Elsevier Ltd., <https://doi.org/10.1016/J.SCS.2021.103540>.
- CEN (Comité Européen for Standardization) (2005). EN 1991-1-4 - Eurocode 1: Actions on Structures - Part 1-4: General actions - Wind Actions, (The European Standard, ed.), Brussels, Belgium.
- CEN (Comité Européen for Standardization) (2022). prEN 1993-1-14 - Eurocode 3: Design of Steel Structures—Part 1–14: Design Assisted by Finite Element Analysis Draft, CEN/TC 250/SC 3 N 3723, Brussels, Belgium.
- Chen, J., J. Y. Zhu, and T. M. Chan, (2020). Experimental and numerical investigation on stub column behaviour of cold-formed octagonal hollow sections, *Eng Struct*, 214 (April): 110669, Elsevier, <https://doi.org/10.1016/J.ENGSTRUCT.2020.110669>.
- Cheung, Y. K., (1976). *Finite Strip Method in Structural Analysis*, 232, Pergamon Press.
- Crisfield, M. A., (1981). A fast incremental/iterative solution procedure that handles ‘snap-through’, *Computational Methods in Nonlinear Structural and Solid Mechanics*, 55–62, Elsevier, [https://doi.org/10.1016/0045-7949\(81\)90108-5](https://doi.org/10.1016/0045-7949(81)90108-5).
- Davenport, A. G., (1967). Gust Loading Factors, *Journal of the Structural Division*, 93 (3): 11–34, <https://doi.org/10.1061/JSDEAG.0001692>.
- Dholakia, R. R., and B. Harlam, (1994). Telecommunications and economic development: Econometric analysis of the US experience, *Telecomm Policy*, 18 (6): 470–477, Pergamon, [https://doi.org/10.1016/0308-5961\(94\)90015-9](https://doi.org/10.1016/0308-5961(94)90015-9).
- Ellobody, E., and B. Young., (2005). Behavior of cold-formed steel plain angle columns, *Journal of Structural Engineering*, 131 (3): 457–466, American Society of Civil Engineers, [https://doi.org/10.1061/\(ASCE\)0733-9445\(2005\)131:3\(457\)](https://doi.org/10.1061/(ASCE)0733-9445(2005)131:3(457)).
- Franco, J. M. S., and E. de M. Batista, (2017). Buckling behavior and strength of thin-walled stiffened trapezoidal CFS under flexural bending, *Thin-Walled Structures*, 117: 268–281, Elsevier, <https://doi.org/10.1016/j.tws.2016.11.027>.
- Godat, A., F. Legeron, and D. Bazonga, (2012). Stability investigation of local buckling behavior of tubular polygon columns under concentric compression, *Thin-Walled Structures*, 53: 131–140, Elsevier, <https://doi.org/10.1016/J.TWS.2011.12.013>.
- Gonçalves, R., and D. Camotim, (2013). Buckling behaviour of thin-walled regular polygonal tubes subjected to bending or torsion, *Thin-Walled Structures*, 73: 185–197, Elsevier, <https://doi.org/10.1016/J.TWS.2013.08.006>.

Hancock, G. J., Y. B. Kwon, and E. Stefan Bernard, (1994). Strength design curves for thin-walled sections undergoing distortional buckling, *J Constr Steel Res*, 31 (2–3), [https://doi.org/10.1016/0143-974X\(94\)90009-4](https://doi.org/10.1016/0143-974X(94)90009-4).

Hancock, G. J., and C. H. Pham, (2022). Finite strip methods for stability analysis of thin-walled members with applications to the Direct Strength Method of design, *Analysis and Design of Plated Structures*, N. E. Shanmugam and C. M. Wang, eds., 177–210, Elsevier, <https://doi.org/10.1016/B978-0-12-823570-6.00011-2>.

Hawkins, D. W., (2010). Discussion of current issues related to steel telecommunications monopole structures, *Structures Congress 2010*, ASCE, ed., 2417–2438. ASCE.

James, W. D., (1976). Effects of Reynolds Number and Corner Radius on Two-Dimensional Flow Around Octagonal, Dodecagonal and Hexdecagonal Cylinders, PhD Thesis, Ames: Iowa State University, Digital Repository.

Lazzari, J. A., and E. M. Batista, (2021). Finite strip method computer application for buckling analysis of thin-walled structures with arbitrary cross-sections, *REM - International Engineering Journal*, 74 (3), <https://doi.org/10.1590/0370-44672020740065>.

Lazzari, J. A. De., (2020). Distortional-Global Interaction in Cold-Formed Steel Lipped Channel Columns: Buckling Analysis, Structural Behavior and Strength, Master Thesis, Rio de Janeiro: Federal University of Rio de Janeiro.

Lazzari, J. A. De, A. R. A. Bicelli, and G. L. X. Da Costa, (2019). Best-performance of cold-formed steel stiffened trapezoidal self-supporting roof members under flexural bending due wind suction pressure (in Portuguese: Configuração de melhor rendimento para telha de aço autoportante submetida à ação de vento de sucção), *Revista de Engenharia Civil IMED*, 6 (2): 130, Complexo de Ensino Superior Meridional S.A., <https://doi.org/10.18256/2358-6508.2019.v6i2.3262>.

Li, Z., (2016). Advanced computational tools for elastic buckling analysis of cold-formed steel structures, *Recent Trends in Cold-Formed Steel Construction*, C. Yu, ed., 109–128, Elsevier, <https://doi.org/10.1016/B978-0-08-100160-8.00005-0>.

Li, Z., J. C. Batista Abreu, J. Leng, S. Ádány, and B. W. Schafer, (2014). Review: Constrained finite strip method developments and applications in cold-formed steel design, *Thin-Walled Structures*, 81: 2–18, Elsevier, <https://doi.org/10.1016/J.TWS.2013.09.004>.

Loredo-Souza, A. M., M. S. Pfeil, E. de L. Nascimento, J. D. Riera, G. F. Fisch, and A. T. Beck, (2022). A climatology-based wind speed map for NBR 6123. *Revista IBRACON de Estruturas e Materiais*, 16 (4): 2023, IBRACON - Instituto Brasileiro do Concreto, <https://doi.org/10.1590/S1983-41952023000400001>.

Martins, A. D., R. Gonçalves, and D. Camotim, (2021). Post-buckling behaviour of thin-walled regular polygonal tubes subjected to bending, *Thin-Walled Structures*, 166: 108106, Elsevier, <https://doi.org/10.1016/J.TWS.2021.108106>.

Matsubara, G. Y., and E. de M. Batista, (2023). Local–distortional buckling mode of steel cold-formed columns: Generalized direct strength design approach, *Thin-Walled Structures*, 183: 110356, Elsevier, <https://doi.org/10.1016/J.TWS.2022.110356>.

Matsubara, G. Y., E. de M. Batista, and G. C. Salles, (2019). Lipped channel cold-formed steel columns under local-distortional buckling mode interaction, *Thin-Walled Structures*, 251–270, Elsevier Ltd., <https://doi.org/10.1016/j.tws.2018.12.041>.

Migita, Y., T. Aoki, and Y. Fukumoto, (1992). Local and Interaction Buckling of Polygonal Section Steel Columns, *Journal of Structural Engineering*, 118 (10): 2659–2676, American Society of Civil Engineers, [https://doi.org/10.1061/\(ASCE\)0733-9445\(1992\)118:10\(2659\)](https://doi.org/10.1061/(ASCE)0733-9445(1992)118:10(2659)).

Odunola, O. O., M. O. Jelili, and M. A. Asani, (2015). Telecommunication mast location and it's health implication for residents in Ogbomoso, Nigeria, *Civil and Environmental Research*, 7 (9): 57–64.

Sabau, G., Koltsakis, E., Lagerqvist, O., (2018). Stability analysis of newly developed polygonal cross-sections for lattice wind towers, *Wind Engineering*, 42(4) 353–363, <https://doi.org/10.1177/0309524X18777366>.

Santos, L. F., (2018). Evaluation of Design Code Procedures for Predicting Building's Aerodynamic Response, Master Thesis (in Portuguese: Avaliação de Métodos Normativos para Determinação da Resposta Aerodinâmica de Edificações), Rio de Janeiro: Civil Engineering Program, Federal University of Rio de Janeiro.

Santos, L. F., F. Guerra, M. S. Pfeil, and R. C. Battista, (2018). Resposta dinâmica de estruturas flexíveis sob a ação de vento segundo a norma brasileira: proposta de novos ábacos (in Portuguese), in: XXXVIII Jornadas Sudamericanas de Ingeniería Estructural, *La Ingeniería Estructural: puente para el desarrollo e integración de América y el mundo*, Lima.

Schafer, B. W., and T. Peköz, (1998). Direct strength prediction of cold-formed steel members using numerical elastic buckling solutions, *International Specialty Conference on Cold-Formed Steel Structures: Recent Research and Developments in Cold-Formed Steel Design and Construction*.

- Schardt, R., (1994). Generalized beam theory—an adequate method for coupled stability problems, *Thin-Walled Structures*, 19 (2–4): 161–180, [https://doi.org/10.1016/0263-8231\(94\)90027-2](https://doi.org/10.1016/0263-8231(94)90027-2).
- Silvestre, N., (2005). *Generalised Beam Theory: New Formulations, Numerical Implementation and Applications*, PhD Thesis (in Portuguese: *Teoria Generalizada de Vigas: Novas Formulações, Implementação Numérica e Aplicações*), Lisbon: Technical University of Lisbon, University of Lisbon.
- Slocum, R., Fairbairn, M., (2015). Slip joints connections: How do these things work?, in: *Electrical Transmission and Substation Structures 2015*, ASME, pp. 363–374, <https://doi.org/10.1061/9780784479414.02>.
- Smith, B., (2009). 50 years in the design of towers and masts. From IASS recommendations to current procedures, *International Association for Shell and Spatial Structures (IASS) Symposium 2009*, A. Domingo Cabo and C. M. Lázaro Fernández, eds., 139–153, Valencia: Editorial Universitat Politècnica de València.
- Solari, G., and L. C. Pagnini, (1999). Gust buffeting and aeroelastic behaviour of poles and monotubular towers, *J Fluids Struct*, 13 (7–8): 877–905, <https://doi.org/10.1006/jfls.1999.0240>.
- Støttrup-Andersen, U., (2009). Masts and towers, *International Association for Shell and Spatial Structures (IASS) Symposium 2009*, A. Domingo Cabo and C. M. Lázaro Fernández, eds., 127–138, Valencia: Editorial Universitat Politècnica de València.
- Szalay, Z., (1989). Drags on several polygon cylinders, *Journal of Wind Engineering and Industrial Aerodynamics*, 32 (1–2): 135–143, [https://doi.org/10.1016/0167-6105\(89\)90024-X](https://doi.org/10.1016/0167-6105(89)90024-X).
- Tang, J. W., Y. M. Xie, P. Felicetti, J. Y. Tu, and J. D. Li., (2013). Numerical simulations of wind drags on straight and twisted polygonal buildings, *The Structural Design of Tall and Special Buildings*, 22 (1): 62–73, John Wiley & Sons, Ltd., <https://doi.org/10.1002/TAL.657>.
- TELEBRÁS S/A., (1997). *Practice -240-410-600: Design procedures for steel self-supporting and cable-stayed towers and poles* (in Portuguese: *Procedimentos de Projeto para Torres Metálicas Auto-Suportadas, Estaiadas e Postes Metálicos*), Brazil.
- Terzaghi, K., (1955). Evaluation of coefficients of subgrade reaction, *Geotechnique*, 5:297-326, <http://dx.doi.org/10.1680/geot.1955.5.4.297>.
- TIA (Telecommunication Industry Association) (2018). *ANSI/TIA-222-H - Structural Standard for Antenna Supporting Structures and Antennas and Small Wind Turbine Support Structures*, Arlington, USA.
- Timoshenko, S., and J. M. Gere., (1963). *Theory of Elastic Stability*, New York: McGraw-Hill.
- Travanca, R., and J. André, (2018). Safety of 5G Network Physical Infrastructures, *A Comprehensive Guide to 5G Security*, 165–193, Wiley, <https://doi.org/10.1002/9781119293071.ch8>.
- Travanca, R., T. de J. Souza, and J. André, (2019). *Structural Safety Assessment of 5G Network Infrastructures*, Wiley 5G Ref, 1–21, Wiley, <https://doi.org/10.1002/9781119471509.w5GRef163>.
- Travanca, R., H. Varum, and P. Vila Real, (2013). The past 20 years of telecommunication structures in Portugal, *Eng Struct*, 48: 472–485, Elsevier, <https://doi.org/10.1016/J.ENGSTRUCT.2012.10.012>.
- Winter, G., *Thin-walled structures: theoretical solutions and test results*, Preliminary Publication of the 8th Congress, IABSE, 1968, pp. 101-12, <https://doi.org/10.5169/seals-8695>.

APPENDIX: Geometric details of reinforcements

Table A.1 Description of the bottom openings with reinforcements and its flexural capacity, from the FEM model results: $b \times h \times t$ angle; $b \times t$ rectangular plate; A_r cross-section area of the reinforcement member; A_p cross-sectional area of the removed element for the opening; $M_{Rk,FE}$ the finite element bending moment strength; M_y the elastic bending moment.

Opening		Reinforcement				Pos. from ground level	A_p	A_r/A_p	$M_{Rk,FE}$	$M_{Rk,FE}/M_y$	$M_{Rk,FE} / M_{Rk,FE,NO}$
Type	Section	b	h	t	A_r						
Figure 10	Type**	mm	mm	mm	mm2	mm	mm2	kNm			
NO	-	-	-	-	-	-	0	0.00	3642	1.02	1.00
(a)	NR	0.0	0.0	0.00	0	400	1422	0.00	2000	0.56	0.55
(a)	RP	63.4	0.0	7.94	1007	400	1422	0.71	2904	0.81	0.80
(a)	L	63.4	63.4	7.94	2014	400	1422	1.42	2822	0.79	0.77
(b)	NR	0.0	0.0	0.00	0	1000	1405	0.00	2038	0.57	0.56
(b)	RP	63.4	0.0	7.94	1007	1000	1405	0.72	2540	0.71	0.70
(b)	L	63.4	63.4	7.94	2014	1000	1405	1.43	2670	0.75	0.73
(b)	L	63.4	63.4	12.70	3221	1000	1405	2.29	2975	0.83	0.82
(b)	L	76.2	76.2	12.70	3871	1000	1405	2.75	2985	0.83	0.82
(b)	L	101.6	101.6	14.29	5807	1000	1405	4.13	3119	0.87	0.86
(b)	L	127.0	127.0	19.05	9677	1000	1405	6.89	3208	0.90	0.88
(b)	L	152.4	152.4	15.88	9680	1000	1405	6.89	3133	0.88	0.86
(b)	L	152.4	152.4	22.22	13545	1000	1405	9.64	3330	0.93	0.91
(c)	RP	63.4	0.0	7.94	1007	1000	1405	0.72	2659	0.74	0.73
(c)	RP	126.8	0.0	7.94	2014	1000	1405	1.43	2702	0.75	0.74
(d)	RP	63.5	0.0	7.94	1008	1000	1080	0.93	2743	0.77	0.75
(d)	RP	72.6	0.0	12.70	1844	1000	1080	1.71	2882	0.81	0.79
(d)	RP	101.6	0.0	14.29	2904	1000	1080	2.69	3003	0.84	0.82
(d)	RP	80.0	0.0	10.00	1600	1000	1080	1.48	2827	0.79	0.78
(e)	RP	70.0	0.0	8.00	1120	1200	1016	1.10	2786	0.78	0.77
(e)	RP	80.0	0.0	10.00	1600	1200	1016	1.57	2860	0.80	0.79
(e)	RP	70.0	0.0	9.53	1334	1200	1016	1.31	2834	0.79	0.78
(e)	RP	140.0	0.0	9.53	2668	1200	1016	2.63	2905	0.81	0.80
(f)	RP	63.5	0.0	7.94	1008	1000	1405	0.72	2611	0.73	0.72
(f)	RP	80.0	0.0	10.00	1600	1000	1405	1.14	2612	0.73	0.72
(f)	*RP	80.0	80.0	10.00	3200	1000	1405	2.28	2784	0.78	0.76
(g)	RP	63.4	0.0	7.94	1007	400	1422	0.71	2966	0.83	0.81
(h)	RP	63.5	0.0	7.94	1008	1000	1113	0.91	2782	0.78	0.76
(h)	RP	80.0	0.0	10.00	1600	1000	1113	1.44	2888	0.81	0.79
(h)	2xRP	63.5	63.5	7.94	2017	1000	1113	1.81	3020	0.84	0.83
(h)	2xRP	70.0	70.0	9.53	2668	1000	1113	2.40	3093	0.86	0.85
(i)	RP	63.4	0.0	7.94	1007	400	1130	0.89	2904	0.81	0.80
(i)	RP	63.4	0.0	7.94	1007	400	1130	0.89	3124	0.87	0.86
(i)	2xRP	70.0	70.0	9.53	2668	400	1130	2.36	3546	0.99	0.97

**NO: Structure without any opening; NR: No reinforcement applied to the opening; L: Angle section with equal legs $b \times h \times t$; RP: Rectangular steel plate $b \times t$; 2xRP: Two sets of rectangular steel plates applied in different regions $b \times h \times t$ (see Figure 9).

* For this specific case, the rectangular plate is applied in both directions, inside and outside of the opening.

Table A.2 Stiffening properties (see Figure 15) and results of 20-sided polygonal cross-section with prismatic geometry $D=1450\text{ mm}$: plate thickness t , geometric dimensions, cross-section area A , critical bending moment M_{cr} and bending moment strength ratio $M_{Rk,DSM} / M_y$.

Stiffener	t (mm)	Numb. of Stiffeners #	w1 or h (mm)	w2 (mm)	φ or β (o)	A (mm ²)	Mcr (kN.m)	MRk,DSM /My
NS	2.65	0	-	-	-	12022	469	0.57
	3.00	0	-	-	-	13610	679	0.62
	3.75	0	-	-	-	17012	1322	0.73
	4.25	0	-	-	-	19281	1920	0.79
	4.75	0	-	-	-	21549	2672	0.85
	6.35	0	-	-	-	28807	6306	1.00
A	2.65	2	6.12	0.00	60	12671	630	0.54
	3.00	2	6.93	0.00	60	14441	933	0.61
	3.75	2	8.66	0.00	60	18311	1876	0.73
	4.25	2	9.81	0.00	60	20949	2770	0.80
	4.75	2	10.97	0.00	60	23633	3912	0.86
	6.35	2	14.66	0.00	60	32532	9205	1.00
B	2.65	1	12.24	71.53	60	12671	1909	0.84
	3.00	1	13.86	70.99	60	14441	2501	0.88
	3.75	1	17.32	69.84	60	18311	4010	0.94
	4.25	1	19.63	69.07	60	20949	5201	0.98
	4.75	1	21.94	68.30	60	23633	6510	1.00
	6.35	1	29.33	65.83	60	32532	11630	1.00
C	2.65	1	56.83	0.00	5.35	12048	1163	0.71
	3.00	1	56.87	0.00	6.06	13648	1658	0.77
	3.75	1	56.96	0.00	7.57	17087	3061	0.88
	4.25	1	57.03	0.00	8.57	19389	4260	0.94
	4.75	1	57.11	0.00	9.58	21700	5617	0.99
	6.35	1	57.42	0.00	12.78	29169	11080	1.00
D	2.65	2	6.12	42.92	60	12671	1177	0.70
	3.00	2	6.93	42.59	60	14441	1669	0.76
	3.75	2	8.66	41.90	60	18311	3059	0.87
	4.25	2	9.81	41.44	60	20949	4183	0.92
	4.75	2	10.97	40.98	60	23633	5409	0.95
	6.35	2	14.66	39.50	60	32532	10330	1.00
E	2.65	2	6.12	42.92	-60	12671	1275	0.72
	3.00	2	6.93	42.59	-60	14441	1830	0.78
	3.75	2	8.66	41.90	-60	18311	3456	0.90
	4.25	2	9.81	41.44	-60	20949	4860	0.95
	4.75	2	10.97	40.98	-60	23633	6458	1.00
	6.35	2	14.66	39.50	-60	32532	11580	1.00
F*	2.65	1	41.82	-	75	12978	753	0.58
	3.00	1	41.82	-	75	14692	1090	0.64
	3.75	1	41.82	-	75	18365	2121	0.76
	4.25	1	41.82	-	75	20813	3078	0.83
	4.75	1	41.82	-	75	23262	4283	0.89
	6.35	1	41.82	-	75	31097	7817	0.98
G	2.65	1	6.12	73.57	60	12346	1455	0.77
	3.00	1	6.93	73.30	60	14025	2017	0.82
	3.75	1	8.66	72.72	60	17662	3512	0.91
	4.25	1	9.81	72.34	60	20115	4711	0.96
	4.75	1	10.97	71.95	60	22591	6071	1.00
	6.35	1	14.66	70.72	60	30670	11370	1.00

Table A.2 Continued...

Stiffener	t	Numb. of Stiffeners	w1 or h	w2	φ or β	A	Mcr	MRk,DSM /My
	(mm)	#	(mm)	(mm)	(o)	(mm ²)	(kN.m)	
G2	2.65	1	6.12	73.57	60	12346	1453	0.76
	3.00	1	6.93	73.30	60	14025	2011	0.82
	3.75	1	8.66	72.72	60	17662	3503	0.91
	4.25	1	9.81	72.34	60	20115	4706	0.96
	4.75	1	10.97	71.95	60	22591	6068	0.99
	6.35	1	14.66	70.72	60	30670	11370	1.00
	H	2.65	1	45.49	45.49	6.69	12055	1366
3.00		1	45.53	45.53	7.57	13657	1875	0.81
3.75		1	45.61	45.61	9.46	17105	3241	0.90
4.25		1	45.69	45.69	10.72	19416	4355	0.95
4.75		1	45.77	45.77	11.98	21738	5633	0.99
6.35		1	46.08	46.08	16.00	29261	10840	1.00

* Vertex stiffener in alternate distribution, $h = w_1$ and $\beta = \varphi$ (see Figure 16(ii)).